

Pathway variability, coat stiffening and mechanical adaptation during clathrin-mediated endocytosis

J. H. H. Dreckhoff, U. S. Schwarz*, L. Lettermann*

BioQuant, Heidelberg University, 69120 Heidelberg, Germany.

Institute for Theoretical Physics, Heidelberg University, 69120 Heidelberg, Germany.

*Corresponding authors. Emails: schwarz@thphys.uni-heidelberg.de and lettermann@uni-heidelberg.de

Clathrin assemblies in cells can persist as flat plaques, abort after partial invagination, or close into clathrin-coated vesicles, but the determinants of these different fates remain unresolved. To investigate the stochastic and complex dynamics of clathrin assemblies, we have developed a kinetic Monte Carlo simulation framework that couples individual clathrin agents to an adaptive continuum membrane. In this hybrid discrete-continuum description, the effective coat bending rigidity and the preferred coat curvature emerge during growth, rather than being prescribed as material parameters. Once connected, curved lattices stiffen from molecular bending modes to coat-level rigidities, because curvature changes require increased stretching or compression, while newly incorporated triskelia hardcode a history-dependent preferred curvature. An analytical theory for non-Euclidean elasticity identifies the relevant internal variables and predicts growth laws that are validated by the simulations. The same microscopic assembly rules yield flat, stalled, and closed coats through two sequential gates in the effective membrane-coat energy landscape. Comparisons with experimentally observed coat geometries and nanodissection-induced curvature changes agree with our theoretical predictions without any fitting parameters. The clathrin coat thus emerges as an adaptive assembly with prestress and memory, whose fate and material parameters reflect the environment in which it has been growing.

Clathrin-mediated endocytosis (CME) is the major route by which eukaryotic cells internalize membrane receptors, nutrients, and signaling molecules. [1, 2, 24, 19, 28, 35] During CME, clathrin triskelia assemble into a polygonal lattice coat that remodels the membrane first into a clathrin-coated pit (CCP) and then into a clathrin-coated vesicle (CCV). [48, 49, 12, 60, 58, 45, 43, 7, 39] Mature coats are far stiffer than individual triskelion legs: measured effective coat rigidities are of order 10^2 – 10^3 $k_B T$, whereas molecular leg bending costs are of order $20 k_B T$. [33, 47, 34, 59] How this mechanical stiffening emerges from the growing lattice and what ultimately drives curvature generation remain unclear, including the question whether pentagonal defects are a cause or a consequence of membrane bending.

Because of their small size, clathrin structures have long been imaged only by electron microscopy. Coated invaginations first appeared as “bristle-coated” pits in thin-

section micrographs [53], followed by the characteristic polygonal basket of pentagons and hexagons [36]; the coat protein was then isolated and named clathrin [49]. Deep-etch electron microscopy gave the first three-dimensional views of coated-pit formation [30], cryo-electron microscopy a pseudo-atomic model of the complete lattice [19], and platinum-replica EM and cryo-electron tomography mapped flat and curved lattices directly at the plasma membrane [58, 45]. More recently, correlated light and electron microscopy [9], super-resolution microscopy [46], and atomic force microscopy [59] have linked lattice state to assembly progress at increasing resolution; Fig. 1A shows an AFM-reconstructed coat from which the lattice geometry can be read off. Single triskelia and the resulting lattice geometry are thus well characterized (Fig. 1B), yet following one coat as it grows in molecular detail remains out of reach. Structural methods require fixed samples and cannot track a single coat over

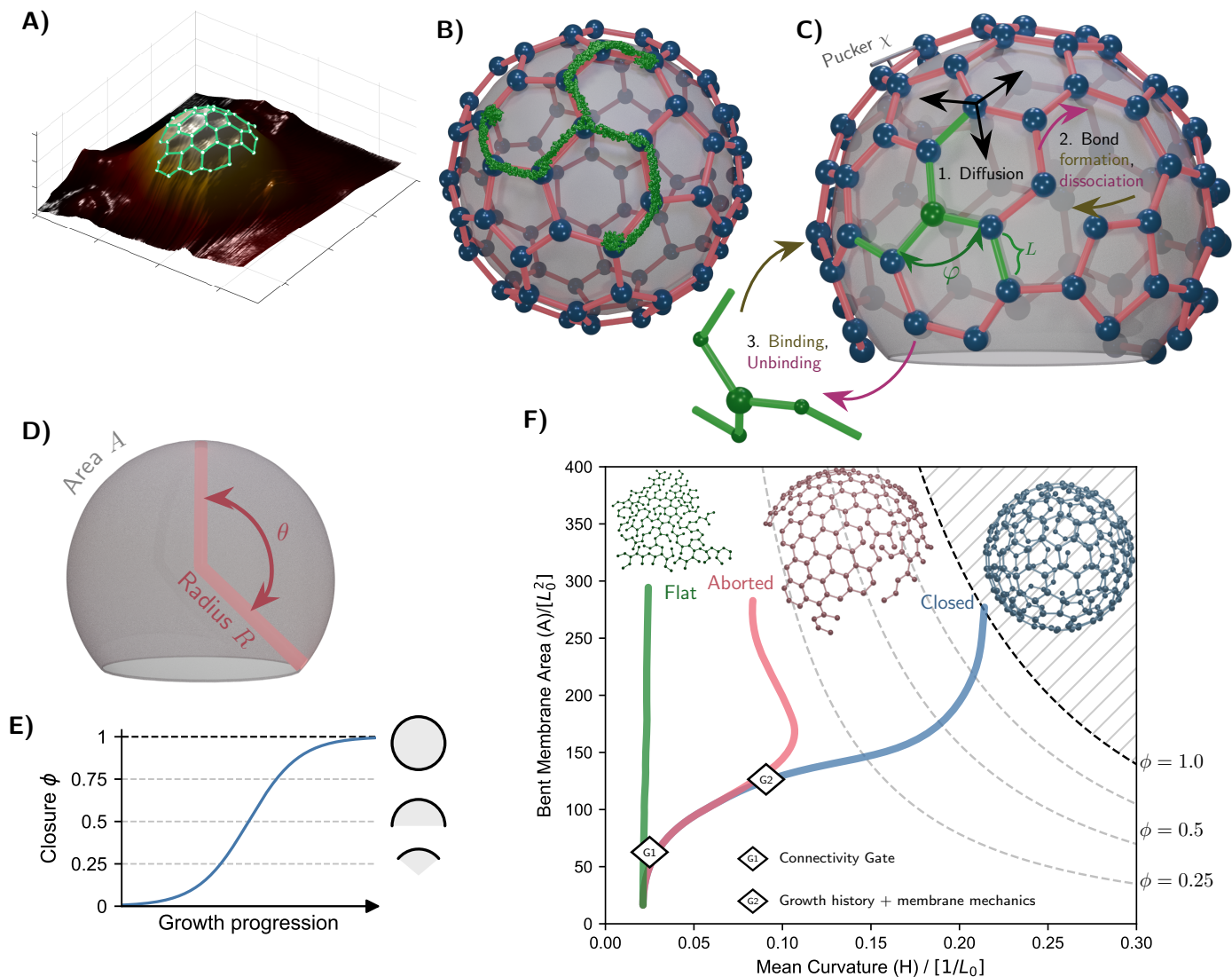


Figure 1: Kinetic Monte Carlo computer simulations explain complex dynamics of clathrin assemblies.

(A) Three-dimensional rendering of a membrane-associated clathrin coat reconstructed from high-speed AFM data, with individual clathrin–clathrin connections highlighted in green. Image reproduced from [59] with permission. (B) Representative simulated coat with a molecular clathrin structure from the Protein Data Bank overlaid onto the lattice. In the simulation, triskelia are represented as discrete mobile nodes connected by deformable legs. (C) Microscopic degrees of freedom and stochastic moves: bound nodes diffuse on the membrane, clathrin–clathrin bonds form and dissociate, and triskelia bind to or unbind from the membrane. The single clathrin state is parameterized by leg length L , in-plane angle ϕ , and pucker angle χ ; binding, unbinding, and bond remodeling are treated as kinetic Monte Carlo events while membrane curvature adapts to the assembly state. (D) Spherical-cap geometry used to couple the two-dimensional coat to membrane curvature, described by area A , radius (inverse curvature) $R = 1/H$, opening angle θ , and closure $\phi = AH^2/4\pi$. (E) Closure ϕ measures the occupied membrane area compared to the total area of a sphere of equal curvature, and will increase for a generic growth process. (F) Area–curvature representation of the three simulated assembly fates: flat plaques (green), aborted pits (pink), and closed coats (blue). Dashed contours indicate lines of constant closure, the shaded region is inaccessible as it lies beyond complete spherical closure ($\phi > 1$), and example simulated coats illustrate the final morphologies. The two fate gates, deciding over the evolution branch, are shown as diamonds.

time [30, 58, 46]; pseudotime ordering of many fixed snapshots approximates an average trajectory [46], but mixes different pathways to final assembly and blurs their differences. Live-cell fluorescence, conversely, follows single sites across their lifetime but resolves neither the molecular lattice nor local curvature or individual binding events [38].

In cells, not every assembly reaches closure: coats are found as persistent flat plaques, aborted pits, or closed vesicles, and what sets these fates remains unclear [58, 46, 9, 63]. Existing models have treated limiting scenarios such as constant-curvature [37] or constant-area [30] growth, and energy-landscape descriptions show how membrane tension and polymerization bias invagination pathways [3, 46, 55, 21]. These frameworks capture much of CME phenomenology, but typically treat coat stiffness and preferred curvature as fixed material parameters rather than as quantities generated by assembly itself. Coat rigidity has recently been proposed to increase dynamically during growth [22], yet a mechanistic framework that bridges microscopic lattice assembly and continuum membrane deformation with dynamical parameters is still missing.

This missing bridge reflects the mixed nature of the problem: membrane bending is a continuum elastic process [29], whereas clathrin assembly is discrete, with individual triskelia binding, diffusing, forming local contacts, leaving vacancies and defects, and ultimately satisfying the topology of a curved trivalent lattice (Fig. 1C) [32, 45, 14, 25]. Since this regime is inaccessible to live-cell imaging, it is a natural target for computer simulation [14]. Earlier simulations, however, imposed coat curvature through prescribed conformational switching of individual triskelia rather than letting it emerge from the assembly energetics, and did not address dynamic coat stiffening, history-dependent curvature memory, or the mechanical selection between flat, aborted, and closed fates.

Here we introduce a hybrid kinetic Monte Carlo model that couples an agent-based clathrin coat to a continuum membrane geometry. Each triskelion is represented as an individual mobile agent on a space-continuous membrane, inspired by the molecular structure (Fig. 1B). Its three legs are coarse-grained into the hub-to-hub-bearing segments that form the lattice. Each agent carries a local elastic Hamiltonian with costs for deviations from the preferred leg length L_0 , in-plane angle φ_0 and pucker angle χ_0 , encoding lateral lattice organization and microscopic curvature preference (Fig. 1C). Nodes diffuse on the membrane, bind and unbind, and form or dissolve clathrin-clathrin contacts with energy-dependent stochastic rates. The hub-to-hub length $L_0 = 18.4$ nm sets the length unit throughout.

Membrane shape enters through a two-dimensional spherical-cap geometry, described by coat area A and

mean curvature H , or, equivalently, by the invagination angle $\cos\theta = 1 - AH^2/2\pi \in [1, -1]$ (Fig. 1D). In the following, we use the more convenient closure variable $\phi = AH^2/4\pi \in [0, 1]$, which is the ratio of occupied membrane area to the area of a sphere of equal curvature. It starts at $\phi = 0$, rises sharply during growth, and plateaus at $\phi = 1$ (Fig. 1E). The molecular degrees of freedom remain surface coordinates, but the surface on which they move can bend, and between stochastic assembly events the membrane curvature adapts adiabatically to the current mechanical state of the coat. The model thereby gives access to the time-resolved microstructural dynamics of coat assembly in a single dynamical framework.

As we will show in the following, from this single model three assembly fates emerge: flat plaques, aborted pits, and closed CCVs, matching the main morphological classes seen experimentally (Fig. 1F), where fate selection proceeds through two sequential gates set by the interplay of discrete and continuum effects. The first gate (G1) is lattice connectivity: coats too poorly connected to transmit coherent bending stresses remain flat, consistent with loose or vacancy-rich flat lattices observed or inferred in cells [58, 20], whereas sufficiently connected coats generate curvature and stiffen through curved spherical assembly. The second gate (G2) is rooted in the continuum energy landscape: for curvature-generating coats the average closure is set by mechanical parameters such as membrane tension, polymerization energy, and membrane bending rigidity, with the surface-tension dependence the clearest signature in the simulations. We find that topological defects such as pentagons and heptagons are not the primary trigger of curvature; rather they follow and stabilize it, reconciling the mechanical pathway with the topological requirement for closed clathrin cages [32, 58, 45]. Combining the simulations with a theory for non-Euclidean elasticity that captures memory and prestress, we identify the underlying growth laws and the precise nature of these gates, and thereby explain the observed pathway variability with one set of physical rules.

Clathrin coats stiffen and develop curvature memory during assembly

We first ask how the mechanical state of a coat changes while the lattice assembles. To isolate lattice mechanics from membrane-shape dynamics, we first grow clathrin at prescribed membrane curvature. This fixed-curvature simulation is experimentally motivated by clathrin assembly on curved membrane templates and by particle-associated uptake geometries, where clathrin and adaptor assemblies respond strongly to local membrane curvature [64, 62]. In

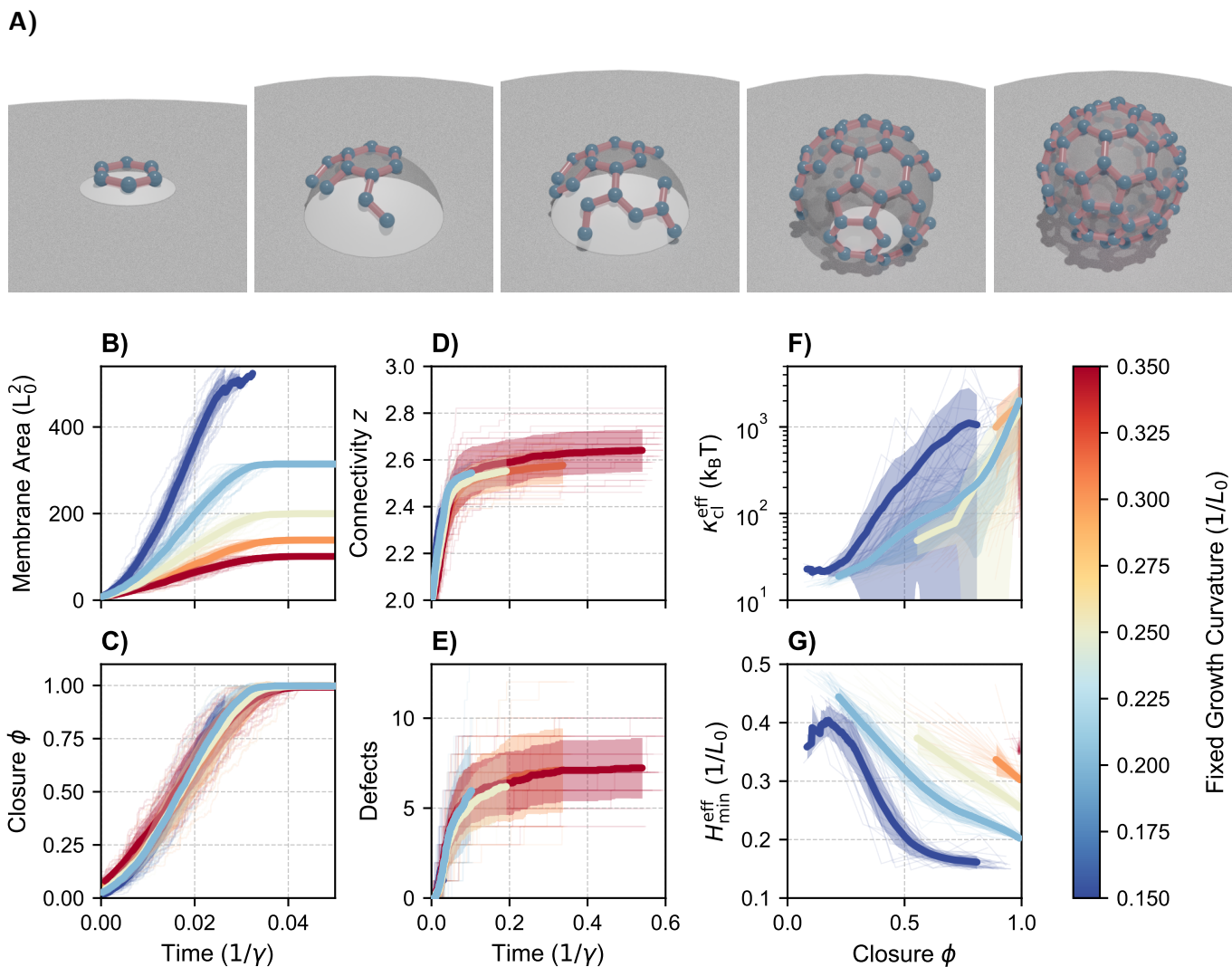


Figure 2: Structural assembly at fixed growth curvature reveals dynamical stiffening and curvature memory. (A) Snapshots of a clathrin lattice growing on a spherical cap with fixed membrane curvature, from early assembly to closure. The membrane is shown in gray, clathrin hubs in blue, and clathrin legs in red. See also Supplementary Movies S1 and S2. (B–G) Growth metrics for ensembles assembled at imposed curvatures from $0.15 L_0^{-1}$ to $0.35 L_0^{-1}$, indicated by color. Thin lines show individual trajectories, thick lines show ensemble means, and shaded regions indicate one standard deviation. Time is given in units of the inverse assembly rate, γ^{-1} . (B) and (C) focus on the early evolution. (B) Clathrin-covered membrane area. Lower-curvature coats occupy larger final areas because the corresponding target sphere is larger. (C) Geometric closure $\phi = AH^2/4\pi$, with $\phi = 1$ marking a closed spherical coat. (D) Mean connectivity z , defined as the average number of clathrin–clathrin bonds per hub. (E) Total number of pentagons plus heptagons, $P + H$, used as a defect-load measure. (F) Effective coat bending rigidity κ_{cl}^{eff} plotted against closure on a logarithmic scale. (G) Effective energy-minimizing curvature H_{min}^{eff} plotted against closure, showing the shift of the preferred coat curvature during growth, with all trajectories ending close to their imposed growth curvature.

the simulation, individual triskelia bind, unbind, diffuse, and remodel bonds on a spherical cap whose curvature is held fixed. The coat therefore assembles on a curved surface, but it does not yet have to bend the membrane itself. Figure 2A shows that compact, ordered trivalent coats emerge from local triskelion rules without imposing a grid, polygon template, or cage architecture.

Figures 2B–G quantify ensembles grown across imposed curvatures from 0.15 to 0.35 L_0^{-1} . We track growth both by time, in units of the inverse microscopic assembly rate γ^{-1} , and by the geometric closure variable $\phi = AH^2/4\pi$, where A is the clathrin-covered area and H is the membrane curvature. Lower-curvature coats require more absolute area to close because their target sphere is larger (Fig. 2B). These coats also grow faster, because they have a larger rim at which new triskelia can dock, in agreement with reaction-limited Eden-type growth models [20]. Rescaled to closure instead of absolute area, trajectories have the same sigmoidal shape for all curvatures (Fig. 2C).

The fixed-curvature simulations also reveal how lattice connectivity evolves when the coat does not have to bend the membrane itself. The mean connectivity z , or coordination number, is the average number of clathrin–clathrin bonds per hub (Fig. 2D). Across imposed curvatures, connectivity follows similar trajectories, although the largest, low-curvature coats remain slightly less connected on average. A natural explanation is geometric crowding: on small, high-curvature caps, triskelia have less lateral space and more readily form nearby contacts, whereas on larger, low-curvature caps, they can assemble more sparsely while still completing the externally prescribed spherical geometry.

Defects provide the corresponding topological readout (Fig. 2E). For an ideal closed trivalent cage on a sphere, Euler topology requires twelve more pentagons than heptagons, $P - H = 12$ [32, 5]. During assembly, the coat is open, has a boundary, and may contain missing bonds, so the closed-cage constraint need not hold at intermediate stages. We therefore plot the total defect load $P + H$, which counts pentagons and heptagons without identifying them with the topological charge. In the fixed-curvature simulation, this defect load rises with time and then plateaus with only weak dependence on imposed curvature, showing that the structural maturation of the lattice is broadly similar across the curvature range.

The mechanical response changes far more strongly. For each assembled coat, we compute an effective coat bending rigidity $\kappa_{\text{cl}}^{\text{eff}}$ by copying the configuration, perturbing its curvature, measuring the energy response, and fitting that response to a Helfrich-type curvature energy. [29]

Because the microscopic parameters are fixed throughout the simulations, changes in $\kappa_{\text{cl}}^{\text{eff}}$ report changes generated by assembly itself. As an overall trend, we observe that at small closure, the coat is compliant, with $\kappa_{\text{cl}}^{\text{eff}}$ of order 20 $k_{\text{B}}T$, comparable to the microscopic leg-bending scale $k_{\text{bend}} \sim 20 k_{\text{B}}T$ listed in Table 1 (detailed derivation of microscopic constants can be found in Supplementary Note 1.1). During growth, the effective coat bending rigidity increases by almost two orders of magnitude and reaches values of order $10^3 k_{\text{B}}T$ near closure (Fig. 2F), placing mature simulated coats in the same broad mechanical regime as experimentally inferred clathrin-coated structures [33, 47, 34, 59]. The final values approach the microscopic stretching scale $k_{\text{stretch}} \sim 800 k_{\text{B}}T$, indicating that the connected coat progressively converts cheap angular rearrangements into costly stretching-dominated resistance. The similar stiffening trajectories across imposed curvatures suggest a common geometric growth law, which we will identify later. Ensemble averages for fitted mechanical quantities are shown only over closure intervals with enough configurations for reliable curvature-response fits; high-curvature coats reach large closure rapidly and therefore contribute shorter reliable fit ranges.

Assembly also changes the curvature that minimizes the overall coat energy. From the same curvature-perturbation fits, we obtain the effective energy-minimizing curvature $H_{\text{min}}^{\text{eff}}$ (Fig. 2G). If this preference were set only by individual triskelion geometry, it would remain close to the microscopic energy-minimizing curvature $H_{\text{min}}^{\text{micro}} \simeq 0.5 L_0^{-1}$, calibrated from clathrin cages assembled in vitro without membrane present [12, 61, 47, 45]. Instead, $H_{\text{min}}^{\text{eff}}$ shifts during growth toward the imposed growth curvature H_{growth} , and the averaged trajectories end close to their respective imposed curvatures. A closed coat grown at fixed curvature has therefore adopted that curvature as its preferred mechanical state.

We interpret this shift as curvature memory. Each newly incorporated triskelion is added in a relaxed configuration at the current membrane curvature and thereby writes a local reference geometry into the growing coat. This is the clathrin analogue of elastic memory in non-Euclidean sheets, where growth or assembly defines local rest distances that need not match a later shape [15, 56, 44, 40]. Fixed-curvature growth thus establishes two assembly-generated state variables, the effective coat bending rigidity $\kappa_{\text{cl}}^{\text{eff}}$ and the effective energy-minimizing curvature $H_{\text{min}}^{\text{eff}}$, which we next allow to feed back onto membrane shape, releasing the previous fixed curvature constraint.

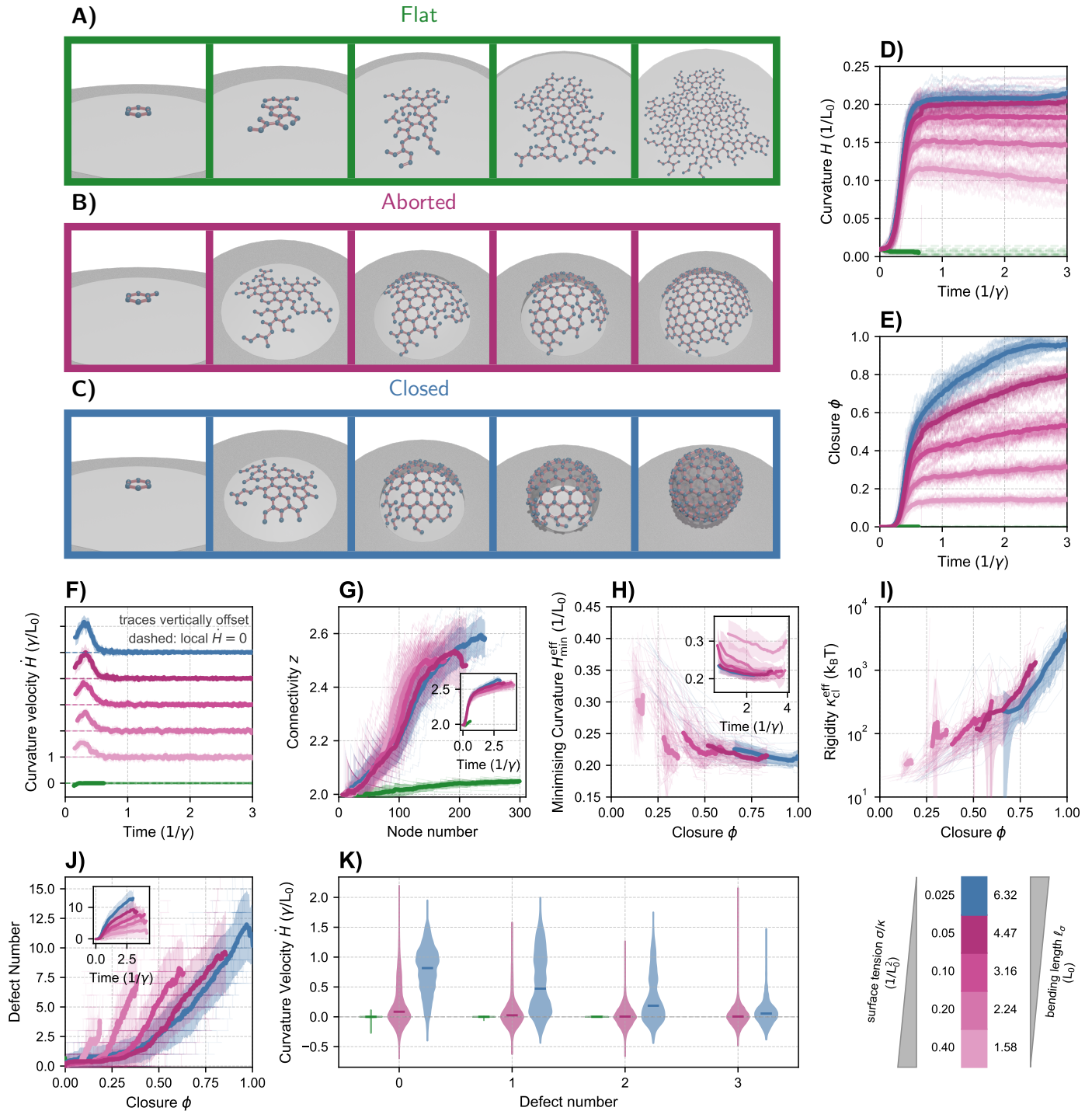


Figure 3: Growth on a deformable membrane produces three assembly fates. (A-C) Representative trajectories of flat, aborted, and closed coats generated by the same microscopic clathrin model. See also Supplementary Movies S3 – S5. (D-K) Growth metrics for assembled coat ensembles with variable curvature during growth. Color indicates final fate, and the pink and blue color scale indicates the membrane bending length $\ell_\sigma = \sqrt{\kappa_M/\sigma}$ or surface tension ratio σ/κ_M , with membrane bending rigidity κ_M and membrane tension σ . (D, E) Membrane curvature and closure during growth show that curvature-generating coats undergo a pronounced bending phase followed by slower evolution; only closed trajectories reach $\phi = 1$. (F) Curvature generation as change in curvature per unit time has a pronounced peak during early development. Different batches shifted in y-direction. (G) Mean connectivity z plotted against the number of incorporated clathrin hubs separates flat plaques from curvature-generating coats, indicating the first fate gate. The inset shows the corresponding time traces. (H)

Effective energy-minimizing curvature H_{\min}^{eff} shows pronounced decrease with closure. The inset shows the corresponding time evolution. **(I)** Effective bending rigidity $\kappa_{\text{cl}}^{\text{eff}}$ again shows increase during growth with closure. **(J)** Defect number plotted against closure. **(K)** Change in membrane curvature per unit simulation time plotted against defect number, showing that curvature can be generated before visible topological defects are present.

Three assembly fates emerge from a minimal model

We next allow membrane shape to evolve with the assembling coat. The simulation now starts from a flat membrane, so curvature is no longer prescribed, but must be produced by the growing lattice itself. Between stochastic clathrin binding, unbinding, diffusion, and bond changes, the spherical-cap curvature adiabatically adapts its mechanical state. We keep the microscopic clathrin parameters fixed and vary the membrane bending length $\ell_{\sigma} = \sqrt{\kappa_{\text{M}}/\sigma}$ which sets the scale at which membrane bending and surface-tension costs balance, by varying the surface tension σ and keeping the membrane bending rigidity κ_{M} fixed. This choice reflects the established role of membrane mechanics in clathrin-coated pit shape and invagination efficiency [55, 9, 27]. We note that in our framework surface tension σ is the main parameter representing the role of the environment on CME, but that other environmental features might also play a role, like adhesion and growth of actin structures.

With the same microscopic assembly rules, the model produces three outcomes: flat plaques, aborted pits, and closed coats (Fig. 3A–C). Importantly, fate is not determined only by the external parameter set. Although the ensemble averages separate clearly with imposed bending length ℓ_{σ} , individual trajectories can reach different outcomes under the same parameters, because their stochastic assembly histories generate different connectivities, growth curvatures, and mechanical states. In this sense, pathway variability is already present at the level of the minimal lattice dynamics.

Flat plaques grow in area but do not generate appreciable curvature. Aborted pits generate curvature but do not complete vesicle closure. Biologically, such abortive outcomes can arise when closure is too slow to occur before coat disassembly, or when the coat reaches a configuration in which further closure is mechanically unfavorable. The finite simulated trajectory length is therefore used only as an operational proxy for the finite cellular lifetime of clathrin-coated pits [42, 54, 10, 25]. Closed coats, in contrast, reach the geometric closure condition $\phi = 1$. The energy-landscape analysis below will separate slowly closing trajectories from trajectories that stall at an internal mechanical state.

The time traces show how the fates separate dynam-

ically (Fig. 3D, E, F). After brief flat growth, curvature-generating coats undergo an initial bending phase, visible as a rapid increase in curvature and closure. Together with a transient peak in the change in curvature per unit simulation time, this represents an emergent flat-to-curved transition. This is followed by a slower phase in which curvature changes little and additional closure is dominated by area growth. The bending length modulates this progression: mechanically resistant membranes show slower curvature generation and lower final closure.

The first structural discriminator is lattice connectivity (Fig. 3G). Plotting the mean connectivity z against the number of incorporated clathrin hubs shows that coats that bend the membrane progressively incorporate hubs with higher connectivity, whereas flat plaques remain sparsely connected as they grow. This suggests a connectivity gate: a coat must become sufficiently connected to transmit bending stresses to the membrane. The result is consistent with experimental and theoretical pictures of loose or vacancy-rich flat clathrin lattices [58, 20, 8]. Because live structural data can show proximity of clathrin legs more directly than mechanical bond strength, we do not equate the simulated value of z with a directly measured cellular quantity. Instead, the model result identifies a necessary mechanical condition: a lattice with too little stress transmission remains flat. Other cellular mechanisms may also weaken or strengthen stress transmission, but some sufficient level of mechanical coupling is required for the geometry-induced stiffening derived below.

Topological defects are not required to initiate curvature generation (Fig. 3J, K). A closed trivalent cage must ultimately satisfy the Euler constraint of twelve excess pentagons, but the simulations show that curvature can start before visible non-hexagonal polygons are counted. Closed trajectories already display large changes in membrane curvature per unit simulation time at zero counted defects. Defects therefore follow and may stabilize curvature generated by a sufficiently connected coat, rather than acting as the primary mechanical trigger [32, 5].

The mechanical state variables identified in the fixed-curvature assay remain dynamic on a deformable membrane. The effective energy-minimizing curvature H_{\min}^{eff} shifts during growth from the microscopic preferred curvature toward the curvature realized by the coat (Fig. 3H), while the effective coat bending rigidity $\kappa_{\text{cl}}^{\text{eff}}$ increases strongly with closure (Fig. 3I). The averages are

shorter than some individual trajectories, because reliable curvature-perturbation fits require enough data points in each fit range, but the qualitative result matches the controlled fixed curvature assay: assembly shifts the effective energy-minimizing curvature of the coat and progressively increases its resistance to curvature changes.

Growth on a deformable membrane therefore converts assembly-written mechanics into fate selection. Low-connectivity coats remain flat; sufficiently connected coats generate curvature; and among these bending trajectories, membrane mechanical load and stochastic growth history determine whether the trajectory stalls before closure or reaches a closed vesicle. We next derive the geometric origin of the stiffening and curvature-memory variables that underlie this branching.

Curved geometry drives stiffening through a bending-to-stretching transition

The fate separation above suggests a mechanical threshold. Once the lattice is connected enough to transmit stress over the coat, curved spherical geometry removes deformation modes that are available to a flat or poorly connected lattice. Loose plaques remain outside this continuum description, whereas connected curved coats can store geometric frustration and convert it into an effective bending stiffness.

The mechanism is illustrated in Fig. 4A. A nearly flat connected patch can change curvature mainly through angular reorientation of clathrin legs, governed by the soft shear scale $\mu \sim k_{\text{angle}} \sim 20 k_B T$. A curved cap is different: changing its curvature changes the metric of a finite spherical patch, and a connected lattice cannot relax this metric change everywhere by shear alone. A residual area strain remains, forcing local compression or stretching and thereby activating the much larger bulk scale $K \sim k_{\text{stretch}} \sim 800 k_B T$. This bending-to-stretching crossover follows the logic of incompatible elastic sheets and non-Euclidean elasticity [15, 56, 44, 40]; the full derivation of a corresponding theory is given in Supplementary Notes 1.2 and 1.3, the connection to non-Euclidean elasticity is made in 1.4, and the main results are explained in the following.

The companion mechanism, curvature memory, is illustrated in Fig. 4B. Each newly incorporated ring of clathrin is added in a mechanically relaxed state at the membrane curvature present at that moment. As the coat subsequently grows and bends the membrane, older material therefore carries a reference geometry written at earlier, usually lower, curvature, whereas newer material carries the reference geometry of later, more curved states. The

energy-minimizing curvature of the assembled coat is thus not only a microscopic property of individual triskelia; it is an accumulated, weighted record of the curvatures at which connected material was added.

For a small spherical patch, a relative curvature strain $e = -\Delta H/H$ leaves a residual dilation $\Xi \simeq -4(\mu/K)e\phi$. This result makes the geometric origin of the effect explicit. In the flat limit, $\phi \rightarrow 0$, a curvature perturbation does not excite the bulk modulus to leading order. At finite closure, the residual dilation grows linearly with ϕ , and the associated stretching energy penalty, $K\Xi^2/2$, grows quadratically. We therefore evaluate the coat energy under a curvature perturbation as a Helfrich-like bending response augmented by the additional dilation-field contribution. Both contributions are quadratic, leading to new, effective parameters for the bending energy: $\kappa_{\text{cl}}^{\text{eff}}$ and $H_{\text{min}}^{\text{eff}}$.

For coats assembled at a fixed growth curvature H_{growth} , the theory reduces to a single geometric weight w ,

$$w = CA^2 H_{\text{growth}}^2 = 4\pi CA\phi, \quad (1)$$

with $C = \mu/(2\pi^2 KL_0^2)$. With the microscopic parameters used here, $C \simeq 1.3 \times 10^{-3} L_0^{-2}$. The predicted effective mechanics are

$$\begin{aligned} \kappa_{\text{cl}}^{\text{eff}} &= \kappa_{\text{bend}}^{\text{micro}} \exp(w), \\ H_{\text{min}}^{\text{eff}} &= (1 - \omega)H_{\text{min}}^{\text{micro}} + \omega H_{\text{growth}}, \end{aligned} \quad (2)$$

where $\omega = w/(1 + w)$ interpolates between the short and long term limits. $\kappa_{\text{bend}}^{\text{micro}} \sim \mu L_0^2 \sim k_{\text{angle}}$ is the microscopic bending scale set by angular deformation of clathrin legs. Thus the same geometric weight stiffens the coat and shifts its effective energy-minimizing curvature from the microscopic value $H_{\text{min}}^{\text{micro}}$ toward the curvature at which the material was assembled. The curvature-memory law is linear in the weight: for $\omega = 0$ the coat retains $H_{\text{min}}^{\text{micro}}$, whereas for $\omega \rightarrow 1$ it approaches H_{growth} . In the fixed-curvature simulations (Fig. 4C), the fitted stiffness trend, $C = (9.87 \pm 0.29) \times 10^{-4} L_0^{-2}$, is close to the prefactor predicted from the independently chosen microscopic parameters μ and K . The nontrivial transformation by $A^2 H_{\text{growth}}^2$ collapses data taken at different imposed curvatures onto a common trend. Deviations are visible mainly for the highest imposed curvatures, where a coat rapidly spans a large fraction of its underlying sphere and the small-patch and quasi-static assumptions are most strongly strained. The transformed energy-minimizing curvatures collapse more tightly onto the predicted weighting variable $\omega = w/(1 + w)$ (Fig. 4D). With this theory, we have identified the physical origin of the sigmoidal growth laws observed in experiments and simulations.

During growth on a deformable membrane, material is incorporated at a sequence of curvatures rather than at

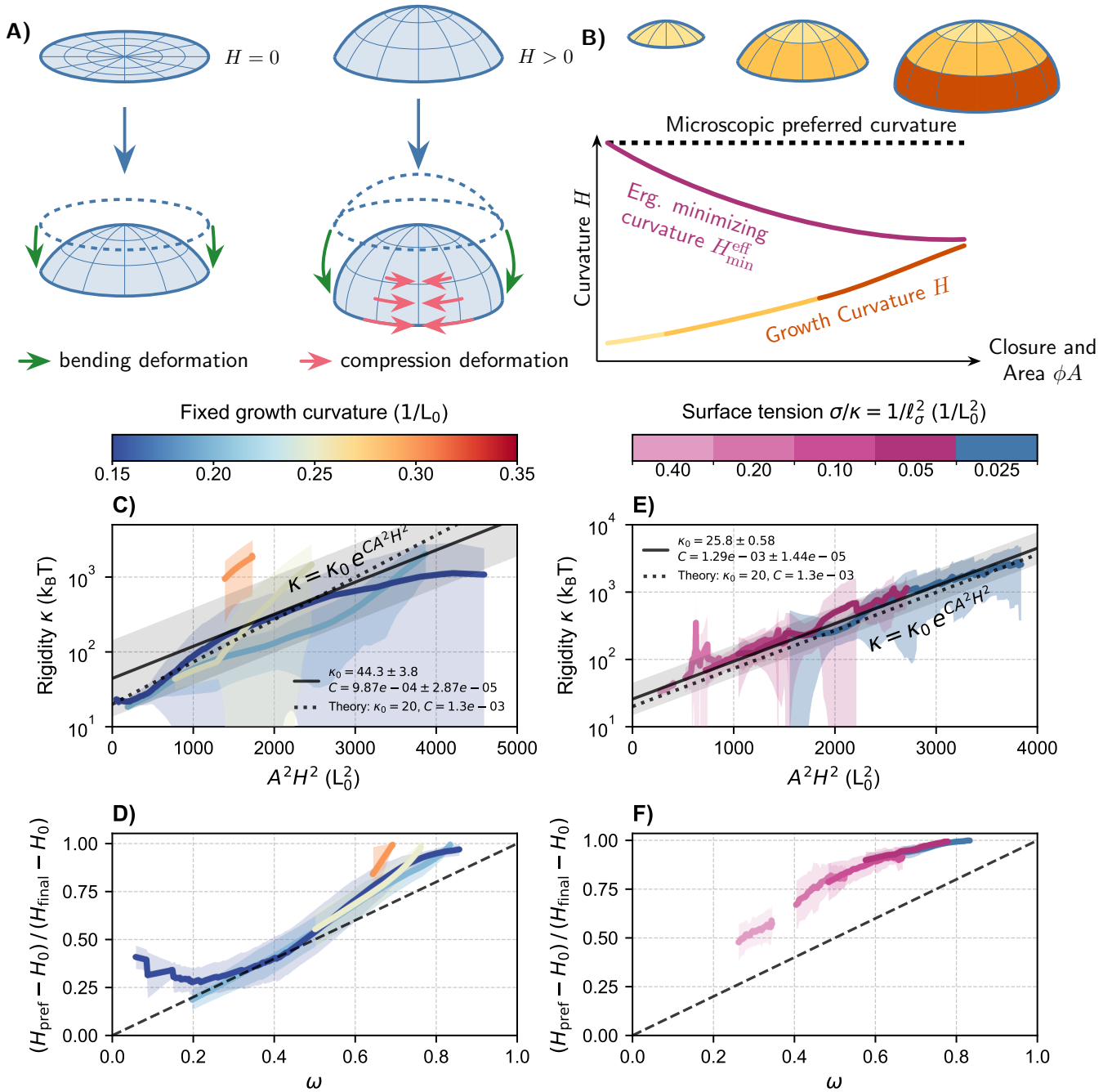


Figure 4: A non-Euclidean theory for geometry-induced stiffening and curvature memory mechanism. (A) Curvature perturbations of a flat connected patch mainly excite angular bending modes, whereas perturbations of a curved cap also require compression or stretching. This geometric constraint produces the bending-to-stretching crossover. (B) During growth, newly incorporated rings are added at the current membrane curvature and thereby store a local reference geometry; the mature coat therefore remembers a weighted average of its growth curvatures. (C, D) Theory and simulation at fixed growth curvature, with colors as in Fig. 2, 1σ error band as shaded region. The transformed effective coat bending rigidity collapses onto the predicted linear trend in (C), and the transformed energy-minimizing curvature follows the predicted weighting variable in (D). Dashed lines show the theoretical prediction and solid lines show simulation fits. (E, F) The same analysis for growth on a deformable membrane, with colors indicating the bending length as in Fig. 3 and the 1σ error band shaded. The stiffness collapse in (E) matches the geometric prediction. In (F), using the final curvature as a proxy for the full curvature history shifts the data relative to the unshifted reference line, as expected for history-weighted curvature memory.

a single H_{growth} . We therefore extend the fixed-curvature result phenomenologically by assigning each incorporated material increment an individual weight w_i and an incorporation curvature H_i . The relevant accumulated quantities are the total stiffening weight and the normalized curvature memory,

$$\mathcal{W} = \sum_i w_i, \quad \mathcal{H} = \frac{\sum_i w_i H_i}{\sum_i w_i}. \quad (3)$$

The effective mechanics then become

$$\begin{aligned} \kappa_{\text{cl}}^{\text{eff}} &= \kappa_{\text{bend}}^{\text{micro}} \exp(\mathcal{W}), \\ H_{\text{min}}^{\text{eff}} &= (1 - \omega) H_{\text{min}}^{\text{micro}} + \omega \mathcal{H}, \end{aligned} \quad (4)$$

with $\omega = \mathcal{W}/(1 + \mathcal{W})$. Curvature memory therefore does not mean that the coat simply remembers its final shape. It remembers the weighted average of the curvatures at which its connected material was added.

The deformable-membrane simulations provide the strongest test of this framework. The same theoretical prefactor computed from μ and K , $C \simeq 1.3 \times 10^{-3} L_0^{-2}$, matches the simulation fit, $C = (1.29 \pm 0.014) \times 10^{-3} L_0^{-2}$ (Fig. 4E). The preferred-curvature collapse is more phenomenological because the full history variable \mathcal{H} is not directly known from the main-figure readout (Fig. 4F). Using the final curvature as a proxy gives the expected offset from the unit-slope reference line while still preserving the predicted trend. Because the final growth curvature is larger than most curvatures sampled during assembly, this rescaling overestimates the history-averaged memory \mathcal{H} and should place the collapsed data above the origin line. The fact that the points nevertheless align on a common line supports the history-weighted memory picture. Together, the collapse of $\kappa_{\text{cl}}^{\text{eff}}$ and the history-dependent shift of $H_{\text{min}}^{\text{eff}}$ show that coat maturation creates the mechanical inputs required for the area–curvature energy landscape introduced next. That also means a shift in the description: the coat is no longer characterized only by its instantaneous area and curvature, but by history-dependent effective parameters that reshape the invagination energy landscape.

Coat connectivity and stiffening control the energy minimum and thereby fate

The stiffening and curvature memory derived above allow us to turn the simulation trajectories into a coarse-grained mechanical picture. We describe an assembling pit by its coated membrane area A and curvature H , and ask how its effective energy landscape $E(A, H)$ changes as the coat matures (Fig. 5). This landscape is not the microscopic KMC Hamiltonian. Instead, it summarizes the many lattice configurations accessible to a coat of a given size and

curvature by two history-dependent material properties: the effective coat bending rigidity $\kappa_{\text{cl}}^{\text{eff}}$ and the effective energy-minimizing curvature $H_{\text{min}}^{\text{eff}}$. In this way, the discrete assembly history derived above becomes a moving continuum description of the invaginating pit. A detailed derivation with explicit calculations is found in Supplementary Note 1.5.

Fig. 5A summarizes the three physical contributions, whose exact form can be found in the Methods. Clathrin polymerization lowers the energy as more triskelia are incorporated and therefore drives growth in area. Membrane bending rigidity κ_{M} and surface tension σ penalize curved and excess membrane area and therefore oppose deep invagination [59, 55]. Clathrin elasticity penalizes deviations from the coat’s current effective energy-minimizing curvature $H_{\text{min}}^{\text{eff}}$, with a strength set by $\kappa_{\text{cl}}^{\text{eff}}$, and is the contribution that changes in strength. The landscape therefore shows how growth, membrane resistance, and coat elasticity compete in the same area–curvature state plane. This connects our model to previous energy-landscape descriptions of endocytic invagination [59, 55, 21].

As the coat matures, the polymerization energy ΔE_{pol} is treated as a fixed microscopic input, while $\kappa_{\text{cl}}^{\text{eff}}$ and $H_{\text{min}}^{\text{eff}}$ evolve with growth history. Early on, energy can be lowered mainly by increasing coated area at low curvature through the polymerization term. Once connectivity and curved geometry generate sufficient coat stiffness, the clathrin elastic term becomes strong enough to reshape the landscape and pull the coat toward higher curvature (Fig. 5A). Coat stiffening therefore does not merely make an already curved coat harder to deform; it shifts the mechanical state that the assembling pit is trying to reach.

At each point along an evolution trajectory, the current values of $\kappa_{\text{cl}}^{\text{eff}}$ and $H_{\text{min}}^{\text{eff}}$ define an instantaneous landscape. Reshaping of this landscape can be expressed as the appearance and movement of an energy minimum at finite area and curvature (Fig. 5B, C). With A_{cl} denoting the mean coated area per incorporated triskelion, a finite basin exists only when the polymerization energy lies within a stiffness-dependent window,

$$\Delta E_{\text{pol}}^{\text{min}} < \Delta E_{\text{pol}} < \Delta E_{\text{pol}}^{\text{max}}, \quad (5)$$

with

$$\Delta E_{\text{pol}}^{\text{max}} = A_{\text{cl}} \left(H_{\text{min}}^{\text{eff}} \right)^2 \kappa_{\text{cl}}^{\text{eff}}, \quad \Delta E_{\text{pol}}^{\text{min}} = \Delta E_{\text{pol}}^{\text{max}} \frac{\kappa_{\text{M}}}{\kappa_{\text{M}} + \kappa_{\text{cl}}^{\text{eff}}}. \quad (6)$$

The full derivation and the corresponding expressions for A_{crit} and H_{crit} , the coordinates of the energy minimum, are given in the Supplement and the Methods respectively. If polymerization is too weak, growth is not favorable ($A, H \rightarrow 0$). If it is too strong, the system can continue

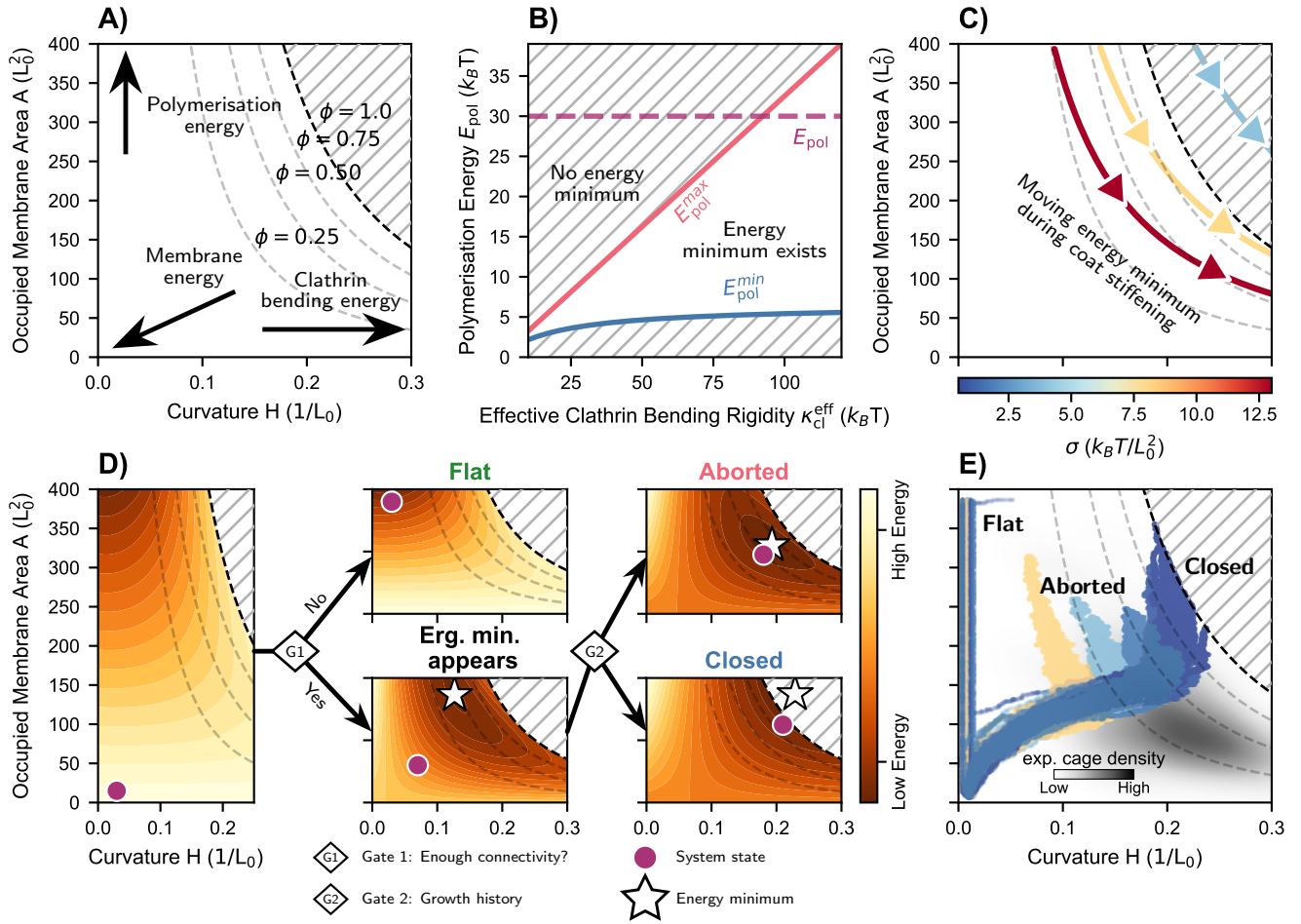


Figure 5: Coat stiffening moves the energy minimum and thereby decides fate. (A) The shape of the energy landscape is controlled by three contributions, the polymerization energy, the membrane bending and surface tension energy, and the clathrin bending energy. The three contributions push the system into three different directions in the curvature-area plane. (B) A finite energy minimum exists only when the polymerization energy per triskelion lies within a stiffness-dependent window. As κ_{cl}^{eff} increases during growth, a fixed polymerization energy can enter this window and create an attractor. (C) For different surface tensions σ , the trajectory of the energy minimum is shifted and crosses the closure line $\phi = 1$ at different points. (D) Energy landscapes at two sequential fate gates. Initially, polymerization energy dominates and the system reduces its energy by expanding area at low curvature. At gate G1 (connectivity), insufficient coat connectivity confines the system to the Flat state; once sufficient connectivity is established, the effective stiffness rises into the window that supports an energy minimum (B), and a minimum appears at finite curvature, redirecting the system toward higher H . The minimum then migrates through the landscape according to surface tension and growth history (C). At gate G2 (growth history), the final fate depends on whether the minimum is reached within the accessible region (Aborted), or crosses the closure boundary before (Closed). (E) Simulated trajectories colored by surface tension σ , with experimentally observed clathrin pits overlaid in gray [59].

lowering its energy by adding area and no finite basin arrests the trajectory; this is the landscape analogue of rapid flat plaque growth when the clathrin term never becomes strong enough to bend the membrane. Increasing κ_{cl}^{eff} moves a fixed ΔE_{pol} into the existence window (Fig. 5B), so a (moving) minimum appears. At fixed ratio of surface tension σ to membrane rigidity κ_M , the trajectory

of the minimum starts at high area and low curvature, and moves with increasing effective bending rigidity κ_{cl}^{eff} towards lower areas and higher curvatures. Increasing σ/κ_M shifts the position of the minimum trajectory to the origin (Fig. 5C).

The three fates emerge from a branched assembly trajectory governed by two sequential fate gates (Fig. 5D).

At early times, polymerization drives area growth, and the energy landscape favors a large, flat coat. The first gate is whether the coat develops sufficient connectivity to enter the stretching-dominated regime: coats that fail to do so remain floppy, continue growing flat, and arrest as persistent plaques. Coats that cross this threshold stiffen, and an energy minimum at finite area and curvature appears in the landscape (Fig. 5B), pulling the system toward an invaginated state. The second gate is determined by a race between the system and its own energy minimum, both of which move through the landscape as the coat stiffens. If the minimum escapes beyond the closure boundary ($\phi = 1$) before the system reaches it, closure is forced; if the system catches its minimum first, it arrests as an aborted pit.

Borderline cases are expected because this landscape is an instantaneous coarse-grained description, not a sharp microscopic phase boundary. As a trajectory approaches its moving minimum, the driving force decreases continuously and closure can slow strongly before motion stops. In biological terms, these coats may still have a weak residual drive toward closure, but not enough to close within the finite lifetime available to an endocytic site. This connects the slow or stalled simulated trajectories to abortive cellular events without treating the simulated observation window as the underlying physical mechanism.

The simulated trajectories in Fig. 5E follow this logic. Lower ratio of membrane surface tension to membrane bending rigidity σ/κ_M , or larger bending length ℓ_σ , shifts the moving minimum so that coats reach higher curvature and more often close; higher tension keeps trajectories closer to the low-curvature region and favors stalling. The experimentally observed pit geometries from [59] overlaid in gray occupy the same order-of-magnitude area-curvature range as the simulated stalled and closing trajectories. They are found at lower areas, because the AFM experiments mainly observe partially closed pits, but agree well with the curvature predicted by our simulations.

In silico cutting validates growth-history and stiffening framework

A direct test of prestress and curvature memory is to perturb an assembled, connected coat. Tagiltsev et al. [59] used HS-AFM nanodissection to cut plasma-membrane-associated clathrin coats and observed relaxation toward increased curvature. We reproduce this logic in silico by selecting coats whose rapid shape evolution has stalled, severing bonds along a radial geodesic from the pole, and then allowing the remaining connected lattice to relax (Fig. 6A). In a typical trajectory, the coat relaxes toward a higher curvature after the cut (Fig. 6B), and the same

tendency is observed across the ensemble (Fig. 6C).

To connect the geometric response to the mechanical framework, we infer κ_{cl}^{eff} and H_{min}^{eff} before and after cutting. The cut consistently reduces the inferred bending rigidity, with an average reduction of roughly 50% (Fig. 6D). At the same time, the inferred energy-minimizing curvature increases (Fig. 6E). Thus cutting does not simply release a stored stress or soften the coat in isolation. It changes both state variables of the growth-history framework: the remaining coat becomes easier to deform, but it also relaxes toward a higher effective energy-minimizing curvature.

The ring-additive theory predicts these two effects. We represent a cut by reducing the weight of the affected material increment, from w_i to $c_i w_i$, where c_i is the retained mechanical fraction of increment i after cutting,

$$w_i \rightarrow c_i w_i, \quad 0 \leq c_i \leq 1. \quad (7)$$

The removed stiffening weight δW and the curvature memory carried by the removed material H_{cut} , with H_i again denoting the incorporation curvature of increment i , are

$$\delta W = \sum_i (1 - c_i) w_i, \quad H_{cut} = \frac{\sum_i (1 - c_i) w_i H_i}{\delta W}. \quad (8)$$

Because the post-cut coat has less accumulated stiffening weight,

$$\Delta \ln \kappa_{cl}^{eff} \simeq -\delta W < 0, \quad (9)$$

so cutting lowers the effective coat bending rigidity. The shift in energy-minimizing curvature is

$$\Delta H_{min}^{eff} \simeq \frac{\delta W}{1 + \mathcal{W}} \left(H_{min}^{eff} - H_{cut} \right). \quad (10)$$

Its sign depends on the curvature memory removed by the cut. If the severed material was incorporated at lower curvature than the intact coat, which is usually the case in the observed assemblies, then $H_{cut} < H_{min}^{eff}$ and cutting increases the effective energy-minimizing curvature. A more detailed derivation is found in Supplementary Note 1.6.

This is the regime sampled by the in silico cuts. They reduce the stress-transmitting weight of the connected lattice while preferentially removing low-curvature memory from earlier growth. The experimental nanodissection response, the first-order theory, and the simulated perturbation therefore agree on the same mechanical interpretation: assembled clathrin coats store growth history in their connected lattice, and cutting reveals this memory by making the coat softer while shifting its relaxed curvature upward.

Discussion

Clathrin assembly has no single morphological endpoint: the same basic coat architecture can remain flat, stall after

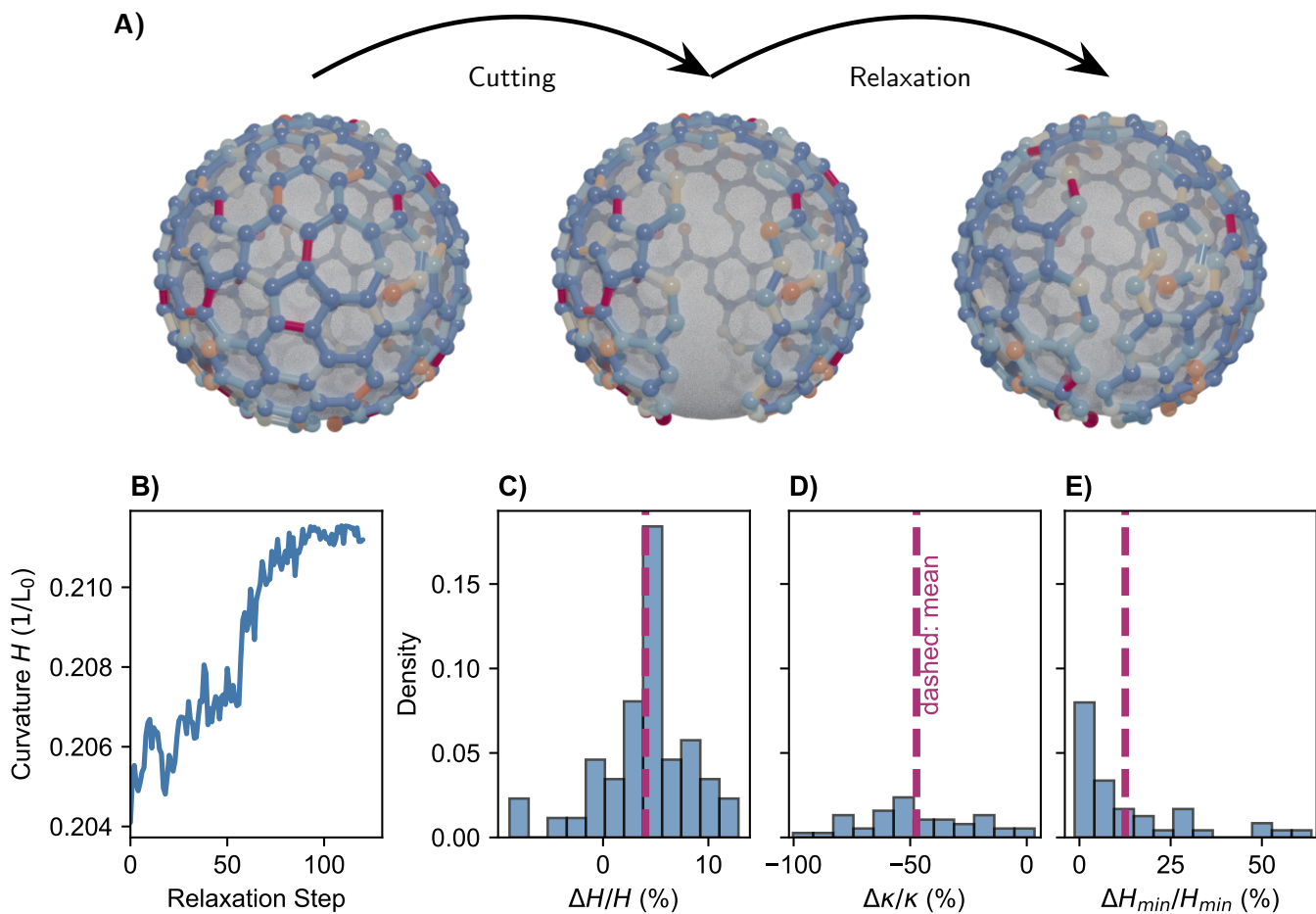


Figure 6: Lattice cutting reduces stiffness and releases curvature memory. (A) In silico cutting protocol: an assembled coat is selected, a radial geodesic is defined, bonds and nodes along the cut are removed, and the remaining connected lattice is allowed to relax. Bond and node colors encode the local energetic load on a logarithmic scale (blue is low, red is high). (B) Example trajectory showing curvature relaxation after cutting. (C) Distribution of relative curvature changes, with a positive mean. (D) Distribution of relative effective bending-rigidity changes, with a negative mean. (E) Distribution of relative preferred-curvature changes, with a positive mean.

partial invagination, or close into a vesicle. A physical theory of CME must therefore explain how one assembling lattice accesses several fates without assigning an independent mechanism to each. Our results identify maturation of coat mechanics as a relevant intermediate layer. During growth, the coat not only accumulates clathrin mass; it changes its capacity to transmit stress, stiffens through geometry, and shifts the curvature it mechanically prefers. Pathway variability can thus arise from the evolving mechanical state of the coat itself. More generally, the discrete effects of self-assembly influence the effective parameters of any continuum description, which can also be expected in other systems, especially if the number of individual agents are small, and finite size effects therefore more important.

Our simulations and theory reevaluate what should be

considered input and output of CME. In many continuum descriptions of CME, coat stiffness and preferred curvature are prescribed, and the membrane shape is then calculated from them. Only recently has it been suggested that a coat rigidity might be a dynamical variable [22], but the underlying microscopic mechanisms were not addressed. Our simulation framework now demonstrates how coat rigidity and preferred curvature are dynamically generated by the interplay of many discrete microscopic processes. It connects constant-curvature models, constant-area models, plaque-derived budding scenarios, and polymerization-tension landscapes [3, 46, 41, 55, 59, 21]: each can be viewed as a limiting description of a lattice whose effective continuum parameters are themselves assembly-generated.

The effective coat bending rigidity emerges from curved spherical geometry. Mature coats are much stiffer

than estimates based on individual triskelion flexibility [33, 47, 34, 59]. In the model, this gap does not require a hidden stiff molecular state. Weakly curved or weakly connected coats can change curvature mainly by angular rearrangement; curved coats necessarily generate residual dilation and compression. The response therefore shifts from bending-dominated to stretching-dominated without changing the microscopic rules.

The effective energy-minimizing curvature is generated at the same time. Each newly incorporated triskelion contributes a local reference geometry set by the curvature at incorporation. The energy-minimizing curvature of the mature coat is therefore encoded in the current mechanical state of the lattice rather than fixed only by molecular architecture. This places clathrin assembly in the broader mechanics of incompatible and growing elastic bodies [15, 56, 44, 40] and offers a physical explanation for why inferred preferred curvatures can vary across cell types, preparations, or mechanical environments.

Fate selection then requires two mechanical steps. First, the coat must transmit stress over the assembly. In the simulation this appears as a connectivity gate, because clathrin-clathrin bonds are the explicit route of stress transmission. Biologically, the same mechanical state could also arise from loose contacts, weak or transient bonds, hidden vacancies, adaptor state, adhesion-associated constraints, or other local regulation. The general prediction is therefore that flat coats fail to transmit coherent bending stresses, not that they must share a universal connectivity threshold.

Second, once stress transmission is possible, fate is set by the moving energy landscape. Geometry-induced stiffening strengthens the clathrin elastic term, curvature memory shifts the energy-minimizing curvature, and membrane mechanics determine whether the evolving minimum stalls inside the accessible region or crosses the closure boundary. The bending length $\ell_\sigma = \sqrt{\kappa_M/\sigma}$ condenses membrane bending rigidity and surface tension into the scale controlling this competition. Molecular regulators enter this framework through membrane load, polymerization gain, lattice coupling, curvature preference, and kinetic rates rather than through a separate theoretical term for every protein.

This view also separates curvature generation from topological completion. A closed trivalent cage must contain twelve excess pentagons [32, 45], but this does not imply that pentagons initiate bending. In the simulations, curvature can begin before visible non-hexagonal polygons are counted, whereas flat lattices can contain defects without curving. Defects are therefore best understood as topological elements that accommodate and stabilize a curved state generated by connected coat mechanics, consistent with observations of flat, defect-containing lattices [58].

The most direct tests are mechanical. Curvature-controlled assembly on beads or curved membrane supports could test whether stiffness increases with coated area and growth curvature. AFM indentation and nanodissection can test whether cutting a connected coat reduces its effective stiffness and shifts its relaxed curvature [59]. Structural methods such as cryo-ET and platinum-replica EM remain essential, but the target is mechanical coupling rather than a universal connectivity value: contact density, vacancies, bond geometry, lattice disorder, and adaptor organization are possible readouts that could be explicitly linked to stress transmission. Controlled tension perturbations should shift stalled and closed outcomes through ℓ_σ [55, 9, 26].

A further theoretical extension would be to relax the spherical-cap constraint. Our simulations describe invagination by a single mean curvature and area, which isolates the role of assembly history but excludes non-spherical deformation modes. Allowing anisotropic deformable pits could further explain how local the curvature memory is, and to what extent the system naturally prefers symmetrical, and hence spherical configurations.

The model presented here demonstrates how the microscopic mechanics of single triskelia alone can lead to macroscopically different cage fates. Cargo, adaptors, epsin, BAR-domain proteins, actin, dynamin, lipid composition, adhesion, turnover, and scission can and will also reshape the effective parameters that control coat maturation and fate. [18, 50, 65] In our treatment, the environment shapes CME through surface tension, but in future extensions, one could include e.g. the effects of adhesion to differently sized cargo or the role of actin networks pushing and pulling on the growing pit.

Our unifying framework demonstrates that physical processes determine the main fate decisions. Because biochemical regulation can shift the balance at these gates, physics and biochemistry will go hand in hand when determining CME fate decisions in different cell types and in different environments. CME should therefore be viewed not as a set of separate pathways for plaques, stalled pits, and vesicles, but as a regulated self-assembly process whose biological diversity is organized by mechanics that is generated by the growth process itself, leading to many feedback loops and high fate variability.

Methods

Individual clathrin bending rigidity

It is possible to infer an estimate for the bending rigidity analogue of a single clathrin. Following the work of Jin and Nossal [33], the flexural rigidity of clathrin arms is $EI_{\text{arm}} \approx 35 \text{ k}_B\text{T nm}$. A coat is formed from units whose arms bind together, so at least two, and at most four arms stick together to form a bond. The flexural rigidity of such a bond is

$$EI_{\text{bond}} = gEI_{\text{arm}}, \quad (11)$$

with $g \in [12, 26]$ for four arms, depending on the geometric arrangement of the arms.

Imagine now a square of clathrin coat of length L_0 . To bend such a square in one direction towards curvature $H = 1/R$ requires bending two such rods, which costs

$$E_{\text{bend,rod}} = \frac{EI_{\text{bond}}L_0}{R^2}. \quad (12)$$

On the other hand, the classical Helfrich picture requires the energy

$$E_{\text{bend,Helfrich}} = \frac{A\kappa}{R^2} \quad (13)$$

with $A = L_0^2$. Equating both yields

$$L_0\kappa = EI_{\text{bond}} \Rightarrow \kappa_{\text{cl}}^{\text{micro}} = g \frac{EI_{\text{arm}}}{L_0}. \quad (14)$$

With $EI_{\text{arm}}/L_0 \approx 1.9 \text{ k}_B\text{T}$ this leaves

$$\kappa_{\text{cl}}^{\text{micro}} \sim 24 - 52 \text{ k}_B\text{T} \quad (15)$$

where one can average this value over the involved legs, leading to $\kappa_{\text{cl}}^{\text{micro}} \sim 6 - 13 \text{ k}_B\text{T}$. A more elaborate derivation can be found in Supplementary Note 1.1.

Microscopic Model

Each clathrin triskelion is represented as a hub at position \mathbf{x} that forms connections ("bonds") to other hubs at positions \mathbf{y} , with Euclidean 3D length $L_y := \sqrt{(\mathbf{x} - \mathbf{y})^2}$. Hubs also form next-nearest-neighbor bonds from \mathbf{y} to \mathbf{z} , of length $L_z := \sqrt{(\mathbf{y} - \mathbf{z})^2}$. Two bonds to direct neighbors, L_i and L_j , enclose a planar angle φ_{ij} , as does each next-nearest-neighbor bond with its proximal leg, and every bond i is tilted out of the local tangent plane by a pucker angle χ_i , see Fig. 1C. The microscopic clathrin energy is

$$E_{\text{bonds}} = \sum_i \left\{ k_{\text{stretch}} \left(\frac{L_i}{L_0} - 1 \right)^2 + k_{\text{bend}} \left[(\chi_i - \chi_0)^2 + (\varphi_i - \varphi_0)^2 \right] \right\}, \quad (16)$$

where the sum runs over formed bonds only. The equilibrium parameters are L_0 , χ_0 and φ_0 : geometry fixes $\varphi_0 = 2\pi/3$, L_0 is clathrin's equilibrium leg length of 18.4 nm, and χ_0 encodes its microscopic preferred curvature.

This energy is coupled to a membrane energy of Helfrich form [29],

$$E_{\text{membrane}} = A\kappa_M H^2. \quad (17)$$

Since the curvature is uniform in our geometry, no integration is required, and the membrane preferred curvature is set to zero. The area A is a weighted mean of $N_{\text{cl}}A_{\text{cl}}$, the number of bound clathrins times the area per clathrin, and $A_{\text{enclosing}}$, the smallest spherical-cap area accommodating all bound clathrins. A polymerization energy ΔE_{pol} is released whenever a previously unbound clathrin first attaches to the membrane.

Evolution algorithm

The dynamics separate into a fast, adiabatic regime and a slow, time-evolving regime. In the fast regime, hub diffusion and curvature adaptation are assumed to remain in quasi-equilibrium and are sampled with a standard Metropolis Monte Carlo algorithm using sufficiently many steps at each instant.

The slow regime drives the physical time evolution through a kinetic Monte Carlo algorithm [57], which assigns a transition rate γ_i to every possible event i . The Gillespie algorithm is a widely used special case [23]. We take each rate to follow an Arrhenius-like law,

$$\gamma_i = \gamma \exp(-\beta \Delta E_i), \quad (18)$$

where ΔE_i is the energy change of process i , γ is a base rate setting the overall time scale, and β is the inverse temperature; we work in units of k_BT , so $\beta = 1$. Clathrin binding events are the exception: because a newly attaching clathrin has a continuum of possible attachment positions, sampling their transition probabilities requires a rejection step [4], at the cost of reduced efficiency.

Implementation

The model is implemented in PYTHON using the JAX library, which provides just-in-time compilation of array programs. [6] A complete kinetic Monte Carlo trajectory, consisting of a fixed number of update steps, is expressed as a single compiled scan over the step index, so that event construction, event sampling, energy evaluation, and the acceptance step are fused into one traced computation rather than dispatched step by step through the Python

Table 1: Experimental values and literature benchmarks for clathrin-mediated endocytosis. Values are taken from the literature or derived from model geometry; entries used as direct simulation inputs are indicated. In the Value column each reported number is immediately followed by its source in square brackets; all sources are collected again in the Reference column. $L_0 = 18.4$ nm is used throughout for unit conversion.

Parameter	Description	Value	References
L_0	Clathrin-clathrin lattice bond length (hub-to-hub); normalization length throughout.	$\sim 18.4 \pm 2.0$ nm	[32, 61, 12]
σ	Membrane tension.	$\sim 1 - 30 \mu\text{N m}^{-1} \approx 0.25 \times 10^{-3} - 7.5 \times 10^{-3} \text{k}_B\text{T nm}^{-2} \approx 0.1 - 2.5 \text{k}_B\text{T } L_0^{-2}$	[13, 51]
κ_M	Membrane bending rigidity.	$\sim 10-25 \text{k}_B\text{T}$, in simulations $\kappa_M = 20 \text{k}_B\text{T}$	[52, 17]
$\kappa_{\text{cl}}^{\text{mature}}$	Bending rigidity of mature clathrin coats/CCVs.	$\sim 100-400 \text{k}_B\text{T}$	[34, 59]
$E I_{\text{arm}}$	Flexural rigidity of one clathrin leg.	$\sim 35 \text{k}_B\text{T nm}$	[33]
k_{bend}	Angular leg bending constant, related to 2D shear modulus $\mu = k_{\text{bend}}/L_0^2$, calibrated to $E I_{\text{arm}}$.	$k_{\text{bend}} = 20 \text{k}_B\text{T}$	[33]
k_{stretch}	Leg stretching constant, related to 2D bulk modulus $K = k_{\text{stretch}}/L_0^2$, calibrated from L_0 fluctuations.	$k_{\text{stretch}} = 800 \text{k}_B\text{T}$	[33]
A_{cl}	Area per triskelion in the coat.	$\sim 433 \text{nm}^2 = 1.28 L_0^2$, in simulations $A_{\text{cl}} = 1.3 L_0^2$	[61, 12]
ΔE_{pol}	Polymerization/binding energy gain per triskelion upon coat incorporation.	$\sim 5-30 \text{k}_B\text{T}$, in simulations $\Delta E_{\text{pol}} = 1 \text{k}_B\text{T}$	[14, 47, 55]
N_{CC}	Number of triskelia in a typical in-vitro clathrin cage.	~ 40	[61]
$R_{\text{CC}}, H_{\text{CC}}$	Radius and mean curvature of in-vitro clathrin cages, microscopic energy-minimizing parameter $H_{\text{min}}^{\text{micro}}$.	$R_{\text{CC}} \approx 30 \text{nm} = 1.63 L_0$; $H_{\text{CC}} \approx 32 \mu\text{m}^{-1} = 0.61 L_0^{-1}$	[61]
N_{CCV}	Number of triskelia in a clathrin-coated vesicle.	$\sim 60-140$	[31]
$R_{\text{CCV}}, H_{\text{CCV}}$	Radius and mean curvature of cellular CCVs/CCPs.	$R_{\text{CCV}} \sim 60-350 \text{nm} = 3.24-19.02 L_0$; $H_{\text{CCV}} \approx 16-2.8 \mu\text{m}^{-1} = 0.30-0.05 L_0^{-1}$	[11, 30, 12]
τ_{CCV}	Mean lifetime of productive CCPs (ending as CCV).	$\sim 30-120$ s	[42, 16]
τ_{abort}	Mean lifetime of aborted (non-productive) CCPs.	$\tau \lesssim 20$ s	[42, 16]

interpreter. Compiling the entire evolution loop in this way, rather than its individual operations, is the principal source of the resulting speedup compared to classical `numpy`. The price of this approach is a more restrictive data layout, because traced computations require array shapes that are fixed at compile time: the lattice is held in node arrays of fixed size, in which unoccupied binding slots are marked by sentinel values, so that the coat grows by activating preallocated entries rather than by resizing arrays. The global simulation state and the node ensemble are registered as JAX pytrees whose definitions separate the dynamic arrays traced during compilation from the static, Python-side configuration, such as node counts and microscopic spring constants. This representation keeps the data structures close to the underlying physical objects while allowing the kinetic Monte Carlo loop to be compiled as a whole and dispatched without modification to either CPU or GPU hardware.

The first execution for a given array shape carries a one-time compilation cost, after which replicate ensembles run at the compiled speed. Each replicate is initial-

ized from a recorded random seed, and all microscopic parameters are read from a tabulated parameter file, so that individual trajectories can be reproduced exactly. The simulations reported here were run on the bwHPC cluster; the 30 variable-curvature trajectories underlying Fig. 3 required between two and four days on a single 64-core node. The complete simulation and analysis pipeline, together with a pinned `conda` environment and a minimal runnable example, is publicly available under the MIT License (see Data and materials availability), and described in more detail in Supplementary Note 2.

Area–curvature landscape

For the coarse-grained invagination analysis, a clathrin-coated pit is described by its coated area A and the mean curvature $H = 1/R$ of a spherical cap. The accessible state space is bounded by the closure condition

$$\phi = \frac{AH^2}{4\pi} \leq 1, \quad A \leq A_{\text{max}}(H) = \frac{4\pi}{H^2}, \quad (19)$$

and the surface-tension term uses the excess area of the cap relative to its projected flat disk, $\Delta A = A^2 H^2 / 4\pi$. This landscape is an effective description rather than the microscopic KMC Hamiltonian: lattice degrees of freedom enter only through the instantaneous $\kappa_{\text{cl}}^{\text{eff}}$ and $H_{\text{min}}^{\text{eff}}$. Normalizing energies by the bending energy $4\pi\kappa_{\text{M}}$ of a closed membrane sphere, the dimensionless landscape reads

$$\mathcal{E}(H, A) = \frac{AH^2}{4\pi} + \frac{\sigma}{\kappa_{\text{M}}} \frac{A^2 H^2}{(4\pi)^2} + \frac{\kappa_{\text{cl}}^{\text{eff}}}{4\pi\kappa_{\text{M}}} (H - H_{\text{min}}^{\text{eff}})^2 A - \frac{\Delta E_{\text{pol}}}{4\pi\kappa_{\text{M}}} \frac{A}{A_{\text{cl}}}, \quad (20)$$

with the four terms representing membrane bending, membrane tension, clathrin bending, and clathrin polymerization. Within a single instantaneous landscape $\kappa_{\text{cl}}^{\text{eff}}$ and $H_{\text{min}}^{\text{eff}}$ are fixed; along a trajectory they evolve as the coat stiffens and develops curvature memory.

At fixed area, $\partial_H \mathcal{E} = 0$ gives the minimizing curvature

$$H^*(A) = \frac{4\pi\kappa_{\text{cl}}^{\text{eff}} H_{\text{min}}^{\text{eff}}}{A\sigma + 4\pi(\kappa_{\text{cl}}^{\text{eff}} + \kappa_{\text{M}})}, \quad (21)$$

and substitution yields the effective one-dimensional energy $\mathcal{E}^*(A) = \mathcal{E}(H^*(A), A)$. A finite-area basin exists only when the polymerization gain lies within the window (cf. Fig. 5)

$$\begin{aligned} \Delta E_{\text{min}} &< \Delta E_{\text{pol}} < \Delta E_{\text{max}}, \\ \Delta E_{\text{max}} &= A_{\text{cl}} (H_{\text{min}}^{\text{eff}})^2 \kappa_{\text{cl}}^{\text{eff}}, \\ \Delta E_{\text{min}} &= \frac{A_{\text{cl}} (H_{\text{min}}^{\text{eff}})^2 \kappa_{\text{cl}}^{\text{eff}}}{1 + \kappa_{\text{cl}}^{\text{eff}} / \kappa_{\text{M}}}, \end{aligned} \quad (22)$$

with corresponding critical curvature and area

$$H_{\text{crit}} = \frac{\sqrt{A_{\text{cl}} (H_{\text{min}}^{\text{eff}})^2 \kappa_{\text{cl}}^{\text{eff}} - \Delta E_{\text{pol}}}}{\sqrt{A_{\text{cl}}} \sqrt{\kappa_{\text{M}} + \kappa_{\text{cl}}^{\text{eff}}}}, \quad (23)$$

$$A_{\text{crit}} = 4\pi\ell_{\sigma}^2 \left[\frac{\kappa_{\text{cl}}^{\text{eff}}}{\kappa_{\text{M}}} \left(\frac{H_{\text{min}}^{\text{eff}}}{H_{\text{crit}}} - 1 \right) - 1 \right], \quad (24)$$

where $\ell_{\sigma} = \sqrt{\kappa_{\text{M}} / \sigma}$. These serve as coarse-grained indicators of whether the moving minimum lies inside the accessible state space or beyond the closure boundary, not as sharp microscopic fate boundaries for individual stochastic KMC trajectories. The full derivation is given in Supplementary Note 1.5.

Deriving geometric stiffening and curvature memory

We model the coat as a continuous small circular patch on a sphere of radius R , i.e. of curvature $H = 1/R$, corresponding to growth at constant curvature. A curvature

strain $e = -\Delta H / H$, with $\Delta H = H' - H$, deforms the patch; the resulting displacement field u_{α} relates to the Cauchy strain tensor $u_{\alpha\beta}$ through

$$u_{\alpha\beta} = \frac{1}{2} (\nabla_{\alpha} u_{\beta} + \nabla_{\beta} u_{\alpha}) + e g_{\alpha\beta}. \quad (25)$$

The last term is the essential ingredient: a change in radius uniformly rescales all distances even when no point moves relative to its surface coordinates. This term can be relaxed away in a flat geometry, but not on the sphere. Its trace $\Xi := \text{tr}(u_{\alpha\beta})$ measures the local area change, i.e. compression or dilation.

With the in-plane elastic energy density

$$\mathcal{U} = \frac{K}{2} \Xi^2 + \mu \tilde{u}_{\alpha\beta} \tilde{u}^{\alpha\beta}, \quad (26)$$

where $\tilde{u}_{\alpha\beta} := u_{\alpha\beta} - \frac{\Xi}{2} g_{\alpha\beta}$ is the trace-free strain and K, μ the two elastic moduli, the equilibrium condition $\nabla_{\beta} \sigma^{\alpha\beta} = 0$ for the stress $\sigma_{\alpha\beta} := \partial \mathcal{U} / \partial u_{\alpha\beta}$ yields the elastostatic equation

$$K \nabla^{\alpha} \Xi + \mu \Delta u^{\alpha} + \frac{\mu}{R^2} u^{\alpha} = 0. \quad (27)$$

Its divergence gives an inhomogeneous Helmholtz equation for Ξ , with an inhomogeneity intrinsic to the curved geometry,

$$\left[\Delta + \frac{1}{\lambda^2} \right] \Xi = \frac{2e}{\lambda^2} \quad \text{with} \quad \lambda := R \sqrt{\frac{K + \mu}{2\mu}}. \quad (28)$$

In the flat limit with azimuthal symmetry, $\Xi \equiv \Xi(r)$ and $\Delta \approx \partial_r^2 + r^{-1} \partial_r$, the general solution of Eq. 28 is

$$\Xi(r) = 2e + C_1 J_0(r/\lambda), \quad (29)$$

with J_0 the zeroth-order Bessel function of the first kind and C_1 fixed by the boundary condition of vanishing radial stress at the patch edge, $\sigma_{rr}(r_{\text{edge}}) = 0$. This gives

$$C_1 \approx -2e \left[1 + \frac{r_{\text{edge}}^2}{4\lambda^2} \right]. \quad (30)$$

In the small-patch limit $J_0(r/\lambda) \approx 1$, so the leading-order curvature dependence of Ξ is carried by the integration constant alone,

$$\Xi \approx -\frac{e r_{\text{edge}}^2}{2\lambda^2} \approx -4 \frac{\mu}{K} e \phi, \quad (31)$$

using $\pi r_{\text{edge}}^2 \approx A$, $\phi = AH^2 / 4\pi$, and $\lambda^2 \approx K / 2\mu H^2$. The detailed calculation can be found in Supplementary note 1.2.

We then split the energy density into a dilation contribution $\mathcal{U}_{\text{dil}} := \frac{K}{2} \Xi^2$ and a bending contribution of Helfrich form [29], $\mathcal{U}_{\text{bend}} \approx \mu(H' - H_{\text{min}}^{\text{micro}})^2$, where H' is the new curvature and $H_{\text{min}}^{\text{micro}}$ is the microscopically preferred curvature. Rearranging,

$$\begin{aligned} \frac{\mathcal{U}}{L_0^2} &= \mu(H' - H_{\text{min}}^{\text{micro}})^2 + \frac{8\mu^2}{KL_0^2} \frac{\phi^2}{H^2} (H' - H)^2 \\ &= (1+w)\mu \left[H' - \frac{H_{\text{min}}^{\text{micro}} + wH}{1+w} \right]^2 \\ \text{with } w &:= \frac{8\mu}{KL_0^2} \frac{\phi^2}{H^2}, \end{aligned} \quad (32)$$

which recovers a standard Helfrich bending energy with the effective parameters

$$\begin{aligned} \kappa^{\text{eff}} &:= (1+w)\mu \approx \exp(w)\mu, \\ H_{\text{min}}^{\text{eff}} &:= \frac{H_{\text{min}}^{\text{micro}} + wH}{1+w}. \end{aligned} \quad (33)$$

For details of the derivation see Supplementary Note 1.2 and 1.3.

References

- [1] R. G. Anderson, M. S. Brown, and J. L. Goldstein. Role of the coated endocytic vesicle in the uptake of receptor-bound low density lipoprotein in human fibroblasts. *Cell*, 10(3):351–364, 1977.
- [2] R. G. W. Anderson, J. L. Goldstein, and M. S. Brown. A mutation that impairs the ability of lipoprotein receptors to localise in coated pits on the cell surface of human fibroblasts. *Nature*, 270(5639):695–699, 1977.
- [3] O. Avinoam, M. Schorb, C. J. Beese, J. A. G. Briggs, and M. Kaksonen. Endocytic sites mature by continuous bending and remodeling of the clathrin coat. *Science*, 348(6241):1369–1372, 2015.
- [4] A. B. Bortz, M. H. Kalos, and J. L. Lebowitz. A new algorithm for Monte Carlo simulation of Ising spin systems. *J. Comput. Phys.*, 17(1):10–18, 1975.
- [5] M. J. Bowick and L. Giomi. Two-Dimensional Matter: Order, Curvature and Defects. *Adv. Phys.*, 58(5):449–563, 2009.
- [6] J. Bradbury, R. Frostig, P. Hawkins, M. J. Johnson, Y. Katariya, C. Leary, D. Maclaurin, G. Necula, A. Paszke, J. VanderPlas, S. Wanderman-Milne, and Q. Zhang. JAX: composable transformations of Python+NumPy programs, 2018.
- [7] F. M. Brodsky. Diversity of Clathrin Function: New Tricks for an Old Protein. *Annu. Rev. Cell Dev. Biol.*, 28(1):309–336, 2012.
- [8] C. P. Broedersz and F. C. MacKintosh. Modeling semiflexible polymer networks. *Rev. Mod. Phys.*, 86(3):995–1036, 2014.
- [9] D. Bucher, F. Frey, K. A. Sochacki, S. Kummer, J.-P. Bergeest, W. J. Godinez, H.-G. Kräusslich, K. Rohr, J. W. Taraska, U. S. Schwarz, and S. Boulant. Clathrin-adaptor ratio and membrane tension regulate the flat-to-curved transition of the clathrin coat during endocytosis. *Nat. Commun.*, 9(1):1109, 2018.
- [10] E. Cocucci, F. Aguet, S. Boulant, and T. Kirchhausen. The First Five Seconds in the Life of a Clathrin-Coated Pit. *Cell*, 150(3):495–507, 2012.
- [11] R. Crowther, J. Pinch, and B. Pearse. On the structure of coated vesicles. *J. Mol. Biol.*, 103(4):785–798, 1976.
- [12] R. A. Crowther and B. M. Pearse. Assembly and packing of clathrin into coats. *J. Cell Biol.*, 91(3):790–797, 1981.
- [13] J. Dai and M. Sheetz. Mechanical properties of neuronal growth cone membranes studied by tether formation with laser optical tweezers. *Biophys. J.*, 68(3):988–996, 1995.
- [14] W. K. Den Otter and W. J. Briels. The Generation of Curved Clathrin Coats from Flat Plaques. *Traffic*, 12(10):1407–1416, 2011.
- [15] E. Efrati, E. Sharon, and R. Kupferman. Elastic theory of unconstrained non-Euclidean plates. *J. Mech. Phys. Solids*, 57(4):762–775, 2009.
- [16] M. Ehrlich, W. Boll, A. Van Oijen, R. Hariharan, K. Chandran, M. L. Nibert, and T. Kirchhausen. Endocytosis by Random Initiation and Stabilization of Clathrin-Coated Pits. *Cell*, 118(5):591–605, 2004.
- [17] E. Evans and W. Rawicz. Entropy-driven tension and bending elasticity in condensed-fluid membranes. *Phys. Rev. Lett.*, 64(17):2094–2097, 1990.
- [18] M. G. J. Ford, I. G. Mills, B. J. Peter, Y. Vallis, G. J. K. Praefcke, P. R. Evans, and H. T. McMahon. Curvature of clathrin-coated pits driven by epsin. *Nature*, 419(6905):361–366, 2002.
- [19] A. Fotin, Y. Cheng, P. Sliz, N. Grigorieff, S. C. Harrison, T. Kirchhausen, and T. Walz. Molecular model for a complete clathrin lattice from electron cryomicroscopy. *Nature*, 432(7017):573–579, 2004.
- [20] F. Frey, D. Bucher, K. A. Sochacki, J. W. Taraska, S. Boulant, and U. S. Schwarz. Eden growth models for flat clathrin lattices with vacancies. *New J. Phys.*, 22(7):073043, 2020.
- [21] F. Frey and U. S. Schwarz. Competing pathways for the invagination of clathrin-coated membranes. *Soft Matter*, 16(47):10723–10733, 2020.
- [22] F. Frey and U. S. Schwarz. Coat stiffening can explain invagination of clathrin-coated membranes. *Phys. Rev. E*, 110(6):064403, 2024.
- [23] D. T. Gillespie. Exact stochastic simulation of coupled chemical reactions. *J. Phys. Chem.*, 81(25):2340–2361, 1977.
- [24] J. L. Goldstein, R. G. W. Anderson, and M. S. Brown. Coated pits, coated vesicles, and receptor-mediated endocytosis. *Nature*, 279(5715):679–685, 1979.

- [25] S. Guo, A. J. Sodt, and M. E. Johnson. Large self-assembled clathrin lattices spontaneously disassemble without sufficient adaptor proteins. *Biophysical Journal*, 121(3):331a, 2022.
- [26] J. E. Hassinger, G. Oster, D. G. Drubin, and P. Rangamani. Membrane tension is a key determinant of bud morphology in clathrin-mediated endocytosis, 2016.
- [27] J. E. Hassinger, G. Oster, D. G. Drubin, and P. Rangamani. Design principles for robust vesiculation in clathrin-mediated endocytosis. *Proc. Natl. Acad. Sci. U.S.A.*, 114(7), 2017.
- [28] V. Haucke and M. M. Kozlov. Membrane remodeling in clathrin-mediated endocytosis. *J. Cell Sci.*, 131(17):jcs216812, 2018.
- [29] W. Helfrich. Elastic Properties of Lipid Bilayers: Theory and Possible Experiments. *Z. Naturforsch. C*, 28(11–12):693–703, 1973.
- [30] J. Heuser. Three-dimensional visualization of coated vesicle formation in fibroblasts. *J. Cell Biol.*, 84(3):560–583, 1980.
- [31] J. Heuser and T. Kirchhausen. Deep-etch views of clathrin assemblies. *J. Ultrastruct. Res.*, 92(1–2):1–27, 1985.
- [32] A. J. Jin and R. Nossal. Topological mechanisms involved in the formation of clathrin-coated vesicles. *Biophys. J.*, 65(4):1523–1537, 1993.
- [33] A. J. Jin and R. Nossal. Rigidity of Triskelion Arms and Clathrin Nets. *Biophys. J.*, 78(3):1183–1194, 2000.
- [34] A. J. Jin, K. Prasad, P. D. Smith, E. M. Lafer, and R. Nossal. Measuring the Elasticity of Clathrin-Coated Vesicles via Atomic Force Microscopy. *Biophys. J.*, 90(9):3333–3344, 2006.
- [35] M. Kaksonen and A. Roux. Mechanisms of clathrin-mediated endocytosis. *Nat. Rev. Mol. Cell Biol.*, 19(5):313–326, 2018.
- [36] T. Kanaseki and K. Kadota. THE "VESICLE IN A BASKET". *J. Cell Biol.*, 42(1):202–220, 1969.
- [37] T. Kirchhausen. Coated pits and coated vesicles — sorting it all out. *Curr. Opin. Struct. Biol.*, 3(2):182–188, Apr. 1993.
- [38] T. Kirchhausen. Imaging endocytic clathrin structures in living cells. *Trends Cell Biol.*, 19(11):596–605, 2009.
- [39] T. Kirchhausen, D. Owen, and S. C. Harrison. Molecular Structure, Function, and Dynamics of Clathrin-Mediated Membrane Traffic. *Cold Spring Harb. Perspect. Biol.*, 6(5):a016725–a016725, 2014.
- [40] Y. Klein, E. Efrati, and E. Sharon. Shaping of Elastic Sheets by Prescription of Non-Euclidean Metrics. *Science*, 315(5815):1116–1120, 2007.
- [41] M. Lampe, S. Vassilopoulos, and C. Merrifield. Clathrin coated pits, plaques and adhesion. *J. Struct. Biol.*, 196(1):48–56, 2016.
- [42] D. Loerke, M. Mettlen, D. Yarar, K. Jaqaman, H. Jaqaman, G. Danuser, and S. L. Schmid. Cargo and Dynamin Regulate Clathrin-Coated Pit Maturation. *PLoS Biol.*, 7(3):e1000057, 2009.
- [43] H. T. McMahon and E. Boucrot. Molecular mechanism and physiological functions of clathrin-mediated endocytosis. *Nat. Rev. Mol. Cell Biol.*, 12(8):517–533, 2011.
- [44] S. Meiri and E. Efrati. Cumulative geometric frustration in physical assemblies. *Phys. Rev. E*, 104(5):054601, 2021.
- [45] K. L. Morris, J. R. Jones, M. Halebian, S. Wu, M. Baker, J.-P. Armache, A. Avila Ibarra, R. B. Sessions, A. D. Cameron, Y. Cheng, and C. J. Smith. Cryo-EM of multiple cage architectures reveals a universal mode of clathrin self-assembly. *Nat. Struct. Mol. Biol.*, 26(10):890–898, 2019.
- [46] M. Mund, A. Tschanz, Y.-L. Wu, F. Frey, J. L. Mehl, M. Kaksonen, O. Avinoam, U. S. Schwarz, and J. Ries. Clathrin coats partially preassemble and subsequently bend during endocytosis. *J. Cell Biol.*, 222(3):e202206038, 2023.
- [47] R. Nossal. Energetics of Clathrin Basket Assembly. *Traffic*, 2(2):138–147, 2001.
- [48] B. M. Pearse. Coated vesicles from pig brain: Purification and biochemical characterization. *J. Mol. Biol.*, 97(1):93–98, 1975.
- [49] B. M. Pearse. Clathrin: A unique protein associated with intracellular transfer of membrane by coated vesicles. *Proc. Natl. Acad. Sci. U.S.A.*, 73(4):1255–1259, 1976.
- [50] B. J. Peter, H. M. Kent, I. G. Mills, Y. Vallis, P. J. G. Butler, P. R. Evans, and H. T. McMahon. BAR Domains as Sensors of Membrane Curvature: The Amphiphysin BAR Structure. *Science*, 303(5657):495–499, 2004.

- [51] D. Raucher and M. P. Sheetz. Cell Spreading and Lamellipodial Extension Rate Is Regulated by Membrane Tension. *J. Cell Biol.*, 148(1):127–136, 2000.
- [52] W. Rawicz, K. Olbrich, T. McIntosh, D. Needham, and E. Evans. Effect of Chain Length and Unsaturation on Elasticity of Lipid Bilayers. *Biophys. J.*, 79(1):328–339, 2000.
- [53] T. F. Roth and K. R. Porter. YOLK PROTEIN UPTAKE IN THE OOCYTE OF THE MOSQUITO AEDES AEGYPTI . L. *J. Cell Biol.*, 20(2):313–332, 1964.
- [54] S. Saffarian, E. Cocucci, and T. Kirchhausen. Distinct Dynamics of Endocytic Clathrin-Coated Pits and Coated Plaques. *PLoS Biol.*, 7(9):e1000191, 2009.
- [55] M. Saleem, S. Morlot, A. Hohendahl, J. Manzi, M. Lenz, and A. Roux. A balance between membrane elasticity and polymerization energy sets the shape of spherical clathrin coats. *Nat. Commun.*, 6(1):6249, 2015.
- [56] E. Sharon and E. Efrati. The mechanics of non-Euclidean plates. *Soft Matter*, 6(22):5693, 2010.
- [57] K. E. Sickafus, E. A. Kotomin, B. P. Uberuaga, and Ettore Majorana Centre for Scientific Culture, editors. *Radiation Effects in Solids: Proceedings of the NATO Advanced Study Institute on Radiation Effects in Solids, 32nd Course of the International School of Solid State Physics, Erice, Sicily, Italy, July, 17-29, 2004*. Number 235 in NATO Science Series /2. Springer Netherland, 2007.
- [58] K. A. Sochacki, B. L. Heine, G. J. Haber, J. R. Jimah, B. Prasai, M. A. Alfonso-Méndez, A. D. Roberts, A. Somasundaram, J. E. Hinshaw, and J. W. Taraska. The structure and spontaneous curvature of clathrin lattices at the plasma membrane. *Dev. Cell*, 56(8):1131–1146.e3, 2021.
- [59] G. Tagiltsev, C. A. Haselwandter, and S. Scheuring. Nanodissected elastically loaded clathrin lattices relax to increased curvature. *Sci. Adv.*, 7(33):eabg9934, 2021.
- [60] E. Ungewickell and D. Branton. Assembly units of clathrin coats. *Nature*, 289(5796):420–422, 1981.
- [61] G. Vigers, R. Crowther, and B. Pearse. Three-dimensional structure of clathrin cages in ice. *EMBO J.*, 5(3):529–534, 1986.
- [62] J. L. Voigt, J. Timmer, F. Pennarola, J. Christian, N. Meng, J. W. Blumberg, U. S. Schwarz, D. Grimm, and E. A. Cavalcanti-Adam. Substrate stiffness and particle properties influence cellular uptake of nanoparticles and viruses from the ventral side. *Adv. Funct. Mater.*, 34(35):2304674, 2024.
- [63] N. M. Willy, J. P. Ferguson, A. Akatay, S. Huber, U. Djakbarova, S. Silahli, C. Cakez, F. Hasan, H. C. Chang, A. Travesset, S. Li, R. Zandi, D. Li, E. Betzig, E. Cocucci, and C. Kural. De novo endocytic clathrin coats develop curvature at early stages of their formation. *Dev. Cell*, 56(22):3146–3159.e5, 2021.
- [64] W. F. Zeno, J. B. Hochfelder, A. S. Thatte, L. Wang, A. K. Gadok, C. C. Hayden, E. M. Lafer, and J. C. Stachowiak. Clathrin senses membrane curvature. *Biophys. J.*, 120(5):818–828, 2021.
- [65] J. Zimmerberg and M. M. Kozlov. How proteins produce cellular membrane curvature. *Nat. Rev. Mol. Cell Biol.*, 7(1):9–19, 2006.

Acknowledgments

We thank G. Tagiltsev and S. Scheuring for providing the rendering for Fig. 1A and the experimental data presented in Fig. 5E. We thank F. Ziebert, F. Frey and N. Winkler for insightful discussions. We acknowledge support by the Deutsche Forschungsgemeinschaft (DFG, German Research Foundation) through Priority Programme 2332 (Projektnummer 492010213) and SFB 1638 (Projektnummer 511488495). We acknowledge support by the state of Baden-Württemberg through bwHPC and the DFG through grant INST 35/1597-1 FUGG, and the scientific data storage service SDS@hd supported by the Ministry of Science, Research and the Arts Baden-Württemberg (MWK) and the DFG through grant INST 35/1503-1 FUGG. AI-assisted technologies: ChatGPT [OpenAI] and Claude [Anthropic] were used solely to improve English wording and readability of author-written text. Coding assistants [GitHub Copilot, Codex & Claude Code] were used to assist with code writing, debugging, and/or refactoring. All AI-assisted text and code were reviewed, edited, tested, and validated by the authors, who take full responsibility for the content, analyses, and results.

Author contributions: U.S.S. and L.L. conceived and supervised the study. J.H.H.D. and L.L. developed the numerical simulation, analysis, and visualization code, and ran the simulations. J.H.H.D. and L.L. conceived the theoretical framework, J.H.H.D. performed the mathematical

derivations. J.H.H.D., U.S.S. and L.L. wrote the paper. All authors reviewed and approved the final version of the paper.

Competing interests: There are no competing interests to declare.

Data and materials availability: The complete simulation code including documentation and the scripts and parameter table to rerun the analysis shown in this paper can be found in the following GitHub repository, after the paper is accepted for publication <https://github.com/Dreckhoff/ClathCoatEvolutionCode>. A detailed description of the repository is also provided in Supplementary Note 2. The original data files for the simulation results are available from the authors upon reasonable request.

Supplementary Materials for Pathway variability, coat stiffening and mechanical adaptation during clathrin-mediated endocytosis

J. H. H. Dreckhoff, U. S. Schwarz*, L. Lettermann*

BioQuant, Heidelberg University, 69120 Heidelberg, Germany.

Institute for Theoretical Physics, Heidelberg University, 69120 Heidelberg, Germany.

*Corresponding authors.

Emails: schwarz@thphys.uni-heidelberg.de and lettermann@uni-heidelberg.de

This PDF file includes:

Supplementary Note 1: Calculations

Supplementary Note 2: Simulation code and reproducibility workflow

Captions for Movies S1 to S6

Other Supplementary Materials for this manuscript include:

Movies S1 to S6

Code repository will be available after acceptance of the manuscript.

1 Calculations

1.1 Calculating the microscopic clathrin bending rigidity and spring constants

This derivation follows closely [3], for general information refer to the classic [5] and [2].

For the transition of bending rigidities we need a value for the individual, single-clathrin bending rigidity. However, in experiment, usually complete clathrin cages are measured. For single clathrin, one observes individual clathrin in solution and tracks its movements.

To model the movement of an individual clathrin arm, we use the theory of elastic rods. There, the bending energy E_{bend} of a rod is given by

$$E_{\text{bend}} = \frac{1}{2}EI \int_0^{s_{\text{tot}}} [C(s) - C_0(s)]^2 ds, \quad (\text{S1})$$

where $C(s)$ is the curvature at arclength s , $C_0(s)$ is the preferred curvature, and EI is called the flexural rigidity with units of length times energy.

Measuring the shape function Ξ and decomposing it into normal modes, $\Xi(s) = \frac{1}{\sqrt{2L}} \sum_{n=0}^{\infty} a_n \cos(n\pi s/L)$, one can extract the flexural rigidity through measurements of the mean

square modes,

$$\langle (a_n - a_n^0)^2 \rangle = \frac{k_B T}{EI} \left(\frac{L}{n\pi} \right)^2, \quad (\text{S2})$$

which yields $EI_{\text{arm}} \approx 35 \text{ k}_B\text{T nm}$ for a single clathrin arm.

In the clathrin coat however, multiple arms bind together to form a bond, at least two, and at most four. For an isotropic and elastic substance, the flexural rigidity may be decomposed as $EI = E \cdot I$, where E is the Young's modulus and I is the moment of inertia. Therefore, the combined flexural rigidity of the clathrin arms is

$$EI_{\text{bond}} = E_{\text{clathrin}} I_{\text{bond}} = E_{\text{clathrin}} (gI_{\text{arm}}) = gEI_{\text{arm}} \quad (\text{S3})$$

where g is a factor depending on the geometric arrangement and number of the arms. Jin and Nossal present different configurations of arms with their resulting factor of g , with $g \in [12, 26]$ with an average of $g \approx 16$, i.e., four bonds do not make the arm four times as stiff, but $4^2 = 16$ times [3].

We can now relate the microscopic flexural rigidity to the bending rigidity of a patch of clathrin to find the single-clathrin analogue to the full-cage bending rigidity. For this, assume we have a patch of clathrin which we want to bend. Then the usual bending energy is

$$E_{\text{bend,membrane}} = \frac{A\kappa_{\text{cl}}}{R^2} \quad (\text{S4})$$

In the other picture, talking about bent rods, two rods need to be bent over their whole length L at curvature $C = 1/R$ to achieve the same overall curvature. There, the bending energy of a single grid cell is

$$E_{\text{bend,rod}} = 2 \frac{1}{2} EI_{\text{bond}} \int_0^L C(s)^2 ds = \frac{EI_{\text{bond}} L}{R^2}. \quad (\text{S5})$$

For a single grid cell, with $A_{\text{gridcell}} \approx L^2$, both equations should match, resulting in

$$\frac{L^2 \kappa_{\text{cl}}}{R^2} = \frac{EI_{\text{bond}} L}{R^2} \quad \Rightarrow \quad \kappa_{\text{cl}} = g \frac{EI_{\text{arm}}}{L} \quad (\text{S6})$$

For a grid cell, $L \approx 18.4 \text{ nm}$, resulting in $EI_{\text{arm}}/L \approx 1.9 \text{ k}_B\text{T}$. Depending on the assumptions taken, this leaves room for $\kappa_{\text{cl}} < 52 \text{ k}_B\text{T}$. Averaging over the involved legs we end up with more realistic values around $\kappa_{\text{cl}} \in [6, 13] \text{ k}_B\text{T}$.

It is of course difficult to assign a precise value. The important note however is that this value is far below the reported $100 - 400 \text{ k}_B\text{T}$ for the full cage bending rigidity!

Related to the single-clathrin bending rigidity is the calculation of the constants for the harmonic potentials governing our microscopic dynamics. For the angles φ and χ , as well as for the length of the legs L , we use harmonic potentials with spring constants k_X (with $X = \varphi, \chi, L$) to constrain the movement.

For convenience, assume that X is given dimensionless and in reference to a preferred value X_0 , i.e. the potential has the form

$$E_X(\Delta X) = k_X(\Delta X)^2, \quad (\text{S7})$$

where we keep with the convention of no factor of $1/2$ in the spring constant for consistency, and $\Delta X = X - X_0$. Let ΔX_{max} be the deviation that is realistically expected to occur. The energy of

such a configuration (including the polymerization energy per leg, $E_{\text{pol.leg}} \approx 5 \text{ k}_B\text{T}$) has to be on the order of the temperature to not be suppressed:

$$E(\Delta X_{\text{max}}) - E_{\text{pol.leg}} \approx \text{k}_B\text{T} = \frac{1}{\beta} \Rightarrow k_X \approx \frac{1 + \beta E_{\text{pol.leg}}}{\beta \Delta X_{\text{max}}^2}. \quad (\text{S8})$$

In units of k_BT , $\beta = 1$. Again from Jin and Nossal [3], the typical order of expected deviations can be taken. For a maximal deviation of $\Delta\varphi_{\text{max}} \approx 0.6 \text{ rad}$ we expect k_φ on the order of $\approx 20 \text{ k}_B\text{T}$. For a maximal deviation of $\Delta L_{\text{max}} \approx 0.1 L_0$ we expect k_L on the order of $\approx 600 \text{ k}_B\text{T}$.

We identify k_φ with the spring constant for angular deviations, and k_L with the spring constant for length deviations. From our experience, we achieved more regular results with a bit higher of a stretching constant, which is why we used a slightly larger value of $k_L = 800 \text{ k}_B\text{T}$.

1.2 Calculating the dilation field and dilation energy

We want to derive how a lattice in a spherical geometry reacts to changes in said geometry. The central result is an analytic expression for the dilation field (measuring how much the lattice is locally compressed or stretched) that accumulates when a coat assembled at curvature H – the growth curvature – is transformed to a curvature H' , and how this dilation field gives rise to the geometry-induced coat stiffening reported in the main text.

Setup and assumptions.

We treat the clathrin coat as a 2D elastic continuum on a spherical surface of radius R , using surface coordinates (r, φ) where r is the geodesic distance from the pole. The metric is diagonal: $g_{rr} = 1$ and $g_{\varphi\varphi} = R^2 \sin^2(r/R)$, and we will be working in standard Riemannian geometry. In the following we list our assumption for the succeeding derivation:

- (A1) *2D continuum elasticity.* The coat is described by a shear modulus μ with $[\mu] = \text{k}_B\text{T}/L_0^2$ and a bulk modulus K with $[K] = \text{k}_B\text{T}/L_0^2$. Both are related to the microscopic spring constants k_{bend} and k_{stretch} describing the microscopic clathrin deformations, with $\mu = k_{\text{bend}}/L_0^2$ and $K = k_{\text{stretch}}/L_0^2$. The shear modulus is a measure of resistance of the coat to shear forces, which is caused by the microscopic angular bending stiffness of the clathrin legs. As a reminder, the typical quantities are $k_{\text{bend}} \sim 20 \text{ k}_B\text{T}$ and $k_{\text{stretch}} \sim 800 \text{ k}_B\text{T}$, thereby $k_{\text{bend}}/k_{\text{stretch}} = \mu/K \ll 1$.
- (A2) *Small strain.* We are working in the limit of small curvature changes, i.e., small strain $|e| = |\Delta H/H| \ll 1$; linearised (Cauchy) elasticity applies.
- (A3) *Small patch.* We will look at a clathrin patch that, at curvature H , only covers a small part of the potential sphere, i.e., the closure $\phi = AH^2/4\pi \ll 1$. Therefore the patch radius satisfies $r_{\text{edge}} \ll R \ll \lambda$, where $\lambda = R\sqrt{(K + \mu)/2\mu} \approx R\sqrt{K/2\mu}$ is the elastic correlation length.
- (A4) *Stress-free boundary.* The radial stress σ_{rr} vanishes at $r = r_{\text{edge}}$, corresponding to a freshly incorporated ring that is mechanically relaxed at its edge.

Strain tensor and elastostatic equilibrium.

Imagine a situation where a spherical patch exists at curvature H , and now the curvature is changed to H' . A change from curvature H to $H' = H + \Delta H$ induces a homogeneous strain $e := \Delta R/R = -\Delta H/H + O((\Delta H/H)^2)$ on the lattice. Let u_α be the displacement field on the sphere, measuring the displacement of any point before and after the curvature change. The Cauchy strain tensor, describing the *relative displacement between neighboring points* (i.e., how much points are locally shifted) is given by

$$u_{\alpha\beta} := \frac{1}{2}(\nabla_\alpha u_\beta + \nabla_\beta u_\alpha) + e g_{\alpha\beta}. \quad (\text{S9})$$

The last summand is what changes compared to a flat geometry. Because different spherical geometries are incompatible, [1] a uniform displacement is forced upon all points. However, a priori this does not need to induce stresses, since the grid could still relax to mitigate this dilation (which is what happens in the flat geometry).

The Cauchy tensor can be decomposed into its trace $\Xi := g^{\alpha\beta}u_{\alpha\beta} = \nabla_\alpha u^\alpha + 2e$ (measuring volume change) and the trace-free shear part $\tilde{u}_{\alpha\beta}$ (measuring shape change),

$$u_{\alpha\beta} = \frac{\Xi}{2} g_{\alpha\beta} + \tilde{u}_{\alpha\beta}. \quad (\text{S10})$$

Then, the in-plane elastic energy density is given by

$$\mathcal{U} = \frac{K}{2} \Xi^2 + \mu \tilde{u}_{\alpha\beta} \tilde{u}^{\alpha\beta} = \mu u_{\alpha\beta} u^{\alpha\beta} + \frac{K-\mu}{2} \Xi^2, \quad (\text{S11})$$

which is the standard isotropic elastic energy for a 2D material. The stress tensor $\sigma^{\alpha\beta} := \partial\mathcal{U}/\partial u_{\alpha\beta} = 2\mu u^{\alpha\beta} + (K - \mu)g^{\alpha\beta}\Xi$ in equilibrium must satisfy $\nabla_\beta \sigma^{\alpha\beta} = 0$, describing force balance at every point (no stress divergence), giving the elastostatic equation

$$K\nabla^\alpha \Xi + \mu \Delta u^\alpha + \frac{\mu}{R^2} u^\alpha = 0, \quad (\text{S12})$$

since

$$\nabla_\beta (g^{\alpha\beta} \Xi) = g^{\alpha\beta} \nabla_\beta \Xi \quad (\text{S13})$$

in Riemannian geometry as $\nabla_\beta g^{\alpha\beta} = 0$ and

$$\begin{aligned} \nabla_\beta u^{\alpha\beta} &= \frac{1}{2} \nabla_\beta \left[\nabla^\alpha u^\beta + \nabla^\beta u^\alpha + \frac{\Delta R}{R} g^{\alpha\beta} \right] \\ &= \frac{1}{2} \left[\nabla_\beta \nabla^\alpha u^\beta + \Delta u^\alpha \right] \\ &= \frac{1}{2} \left(\left[\nabla^\alpha \nabla_\beta + R^\alpha_\beta \right] u^\beta + \Delta u^\alpha \right) \\ &= \frac{1}{2} \left(\nabla^\alpha \Xi + \frac{1}{R^2} u^\alpha + \Delta u^\alpha \right) \end{aligned} \quad (\text{S14})$$

where we used the Ricci-identity for swapping the covariant derivatives, used that the Ricci tensor in our coordinates is $R^\alpha_\beta = \delta^\alpha_\beta/R^2$. and used that $\nabla^\alpha (\nabla_\beta u^\beta) = \nabla^\alpha (\nabla_\beta u^\beta + 2\Delta R/R) = \nabla^\alpha \Xi$.

Explicit divergence of the elastostatic equation.

We now spell out the step in which a second covariant divergence is applied to Eq. (S12). Acting with ∇_α gives

$$K\Delta\Xi + \mu \nabla_\alpha \Delta u^\alpha + \frac{\mu}{R^2} \nabla_\alpha u^\alpha = 0. \quad (\text{S15})$$

The only non-trivial term is the divergence of the vector Laplacian. On a sphere of constant radius R , commuting the derivatives once gives

$$\nabla_\alpha \Delta u^\alpha = \nabla_\alpha \nabla_\beta \nabla^\beta u^\alpha = \Delta(\nabla_\alpha u^\alpha) + R_{\alpha\beta} \nabla^\alpha u^\beta. \quad (\text{S16})$$

Here $R_{\alpha\beta} = g_{\alpha\beta}/R^2$, so the curvature term is simply

$$R_{\alpha\beta} \nabla^\alpha u^\beta = \frac{1}{R^2} g_{\alpha\beta} \nabla^\alpha u^\beta = \frac{1}{R^2} \nabla_\alpha u^\alpha. \quad (\text{S17})$$

With $q := \nabla_\alpha u^\alpha$, Eq. (S15) therefore becomes

$$K\Delta\Xi + \mu \left(\Delta q + \frac{q}{R^2} \right) + \frac{\mu}{R^2} q = 0. \quad (\text{S18})$$

The trace definition $\Xi = \nabla_\alpha u^\alpha + 2e$ implies $q = \Xi - 2e$. Since the imposed geometric strain $e = \Delta R/R$ is spatially constant for a homogeneous change of sphere radius, $\Delta q = \Delta\Xi$. Substituting this into Eq. (S18) gives

$$(K + \mu)\Delta\Xi + \frac{2\mu}{R^2}(\Xi - 2e) = 0. \quad (\text{S19})$$

Dividing by $K + \mu$ and defining $\lambda^{-2} := 2\mu/[R^2(K + \mu)]$ yields the *inhomogeneous Helmholtz equation* for the dilation field:

$$\left[\Delta + \frac{1}{\lambda^2} \right] \Xi = \frac{2e}{\lambda^2}, \quad \lambda := R \sqrt{\frac{K + \mu}{2\mu}} \approx R \sqrt{\frac{K}{2\mu}}. \quad (\text{S20})$$

Solution in the small-patch limit.

Assuming azimuthal symmetry ($\Xi \equiv \Xi(r)$) and invoking assumption (A3), the small patch size, the Laplacian can be approximated by its flat-space form $\Delta \approx \partial_r^2 + r^{-1}\partial_r$, since the essential feature of spherical geometry is the inhomogeneity. The general solution of Eq. (S20) is

$$\Xi(r) = 2e + C_1 J_0(r/\lambda), \quad (\text{S21})$$

where J_0 is the zeroth-order Bessel function of the first kind and C_1 is set by condition (A4).

Using the azimuthal symmetry, the only non-vanishing Christoffel symbols (reminder: $\nabla_\alpha u^\beta := \partial_\alpha u^\beta + \Gamma_{\alpha\lambda}^\beta u^\lambda$ and $\nabla_\alpha u_\beta := \partial_\alpha u_\beta - \Gamma_{\alpha\beta}^\lambda u_\lambda$) are $\Gamma_{\varphi\varphi}^r = -R \sin(r/R) \cos(r/R)$ and $\Gamma_{r\varphi}^\varphi = \cos(r/R)/R$. Therefore we find

$$u_{rr} = \nabla_r u_r + e g_{rr} = \partial_r u_r + e \quad (\text{S22})$$

and

$$u_{\phi\phi} = \nabla_\phi u_\phi + e g_{\phi\phi} = R \sin\left(\frac{r}{R}\right) \cos\left(\frac{r}{R}\right) u_r(r) + e R^2 \sin^2\left(\frac{r}{R}\right) \quad (\text{S23})$$

The dilation, as the trace of the Cauchy tensor, is simply the sum of both terms combined using the inverse metric, leading to

$$\begin{aligned}
\Xi &= \text{tr}(u_{\alpha\beta}) = g^{\alpha\beta} u_{\alpha\beta} \\
&= \partial_r u_r + e + \frac{1}{R^2 \sin^2\left(\frac{r}{R}\right)} u_{\phi\phi} \\
&= 2e + \partial_r u_r + \frac{u_r(r)}{R} \cot\left(\frac{r}{R}\right) \\
&\approx 2e + \partial_r u_r + \frac{u_r(r)}{r} \quad @ \quad r \ll R
\end{aligned} \tag{S24}$$

Using $\partial_r(ru_r)/r = \partial_r u_r + u_r/r$, we find

$$\Xi = 2e + \frac{1}{r} \partial_r (u_r r). \tag{S25}$$

Using the solution for $\Xi(r) = 2e + C_1 J_0(r/\lambda)$, we find

$$\frac{1}{r} \frac{d}{dr} (ru_r) = C_1 J_0(r/\lambda) \Rightarrow \frac{ru_r}{C_1} = \int dr r J_0(r/\lambda) = \lambda r J_1(r/\lambda) + C_2 \tag{S26}$$

using $\int x J_0(x) dx = x J_1(x)$. Finiteness at $r = 0$ dictates $C_2 = 0$, giving us

$$u_r(r) = \lambda C_1 J_1(r/\lambda) \tag{S27}$$

The radial stress at the patch edge is

$$\begin{aligned}
\sigma_{rr} &= 2\mu u_{rr} + (K - \mu)\Xi \\
&= 2\mu (\partial_r u_r + e) + (K - \mu) (2e + C_1 J_0(r/\lambda)) \\
&= 2\mu (\partial_r (\lambda C_1 J_1(r/\lambda)) + e) + (K - \mu) (2e + C_1 J_0(r/\lambda)) \\
&= 2\mu \left[C_1 \left(J_0(r/\lambda) - \frac{\lambda}{r} J_1(r/\lambda) \right) + e \right] + (K - \mu) (2e + C_1 J_0(r/\lambda)) \\
&= 2Ke + C_1 \left[(K + \mu) J_0(r/\lambda) - \frac{2\mu\lambda}{r} J_1(r/\lambda) \right]
\end{aligned} \tag{S28}$$

Then

$$\sigma_{rr}(r_{\text{edge}}) = 2Ke + C_1 \left[(K + \mu) J_0^{\text{edge}} - \frac{2\mu\lambda}{r_{\text{edge}}} J_1^{\text{edge}} \right], \tag{S29}$$

where $J_n^{\text{edge}} := J_n(r_{\text{edge}}/\lambda)$. Setting $\sigma_{rr}(r_{\text{edge}}) = 0$ and expanding in $r_{\text{edge}}/\lambda \ll 1$ (assumption A3) gives $C_1 \approx -2e[1 + r_{\text{edge}}^2/4\lambda^2]$. For a qualitative understanding of the behaviour, it suffices to substitute back into Eq. (S21) and retain the leading order in r_{edge}/λ ,

$$\Xi \approx -\frac{e r_{\text{edge}}^2}{2\lambda^2} \quad (r \ll R \ll \lambda). \tag{S30}$$

Using $\pi r_{\text{edge}}^2 \approx A$ and $\phi = AH^2/4\pi$, the geometric prefactor is rewritten in terms of closure to give the key result:

$$\boxed{\Xi(\phi) \approx -4 \frac{\mu}{K} e \phi.} \quad (\text{S31})$$

Equation (S31) has a transparent physical interpretation: a curvature change produces a total strain e ; most of it is absorbed by cheap in-plane shear (modulus μ), but a residual dilation proportional to ϕ cannot be accommodated because the compact spherical geometry progressively constrains planar rearrangements as coverage grows. For $\phi \rightarrow 0$ (flat plaque), $\Xi \rightarrow 0$: shear suffices and no stiffening occurs.

Dilation energy and stiffening.

For a patch undilated at closure ϕ , the energy density from the bulk modulus $\mathcal{U}_{\text{dil}} = \frac{K}{2}\Xi^2$ can be used to construct an effective energy. We first consider the case where the connected coat is grown at a single curvature H . This is the fixed-growth-curvature protocol used in Fig. 2 of the main text.

We combine the dilation energy with the shear deformation energy from μ , expressed in the usual Helfrich-type form using $\kappa = \mu L_0^2$,

$$\Xi(H'; H) = -4 \frac{\mu}{K} e \phi, \quad e = -\frac{H' - H}{H}. \quad (\text{S32})$$

Using this connected-coat amplitude for the stiffness matching gives the dilation contribution

$$\begin{aligned} \frac{\mathcal{U}_{\text{dil}}}{L_0^2} &= \frac{K}{2L_0^2} \Xi^2(H'; H) \\ &= \frac{8\mu^2}{KL_0^2} \frac{\phi^2}{H^2} (H' - H)^2. \end{aligned} \quad (\text{S33})$$

The total effective energy is therefore

$$\frac{\mathcal{U}_{\text{tot}}}{L_0^2} = \mu (H' - H_{\text{min}}^{\text{micro}})^2 + \frac{\mathcal{U}_{\text{dil}}}{L_0^2}. \quad (\text{S34})$$

Substituting Eq. (S33) yields

$$\begin{aligned} \frac{\mathcal{U}_{\text{tot}}}{L_0^2} &= \mu (H' - H_{\text{min}}^{\text{micro}})^2 + \frac{8\mu^2}{KL_0^2} \frac{\phi^2}{H^2} (H' - H)^2 \\ &= \mu \left[(H')^2 - 2H'H_{\text{min}}^{\text{micro}} + H_{\text{min}}^{\text{micro}2} + \frac{8\mu}{KL_0^2} \frac{\phi^2}{H^2} \left((H')^2 - 2H'H + H^2 \right) \right] \\ &= \mu \left[(1+w)(H')^2 - 2H'(H_{\text{min}}^{\text{micro}} + wH) + H_{\text{min}}^{\text{micro}2} + wH^2 \right] \\ &= (1+w)\mu \left[H' - \frac{H_{\text{min}}^{\text{micro}} + wH}{1+w} \right]^2 + \text{const.} \end{aligned} \quad (\text{S35})$$

where

$$w := \frac{8\mu \phi^2}{KL_0^2 H^2} = \frac{2\mu}{\pi KL_0^2} A\phi = \frac{\mu}{2\pi^2 KL_0^2} A^2 H^2 := C A^2 H^2. \quad (\text{S36})$$

Thus

$$C = \frac{\mu}{2\pi^2 KL_0^2}. \quad (\text{S37})$$

The effective bending rigidity and preferred curvature are therefore

$$\kappa^{\text{eff}} = (1 + w)\kappa \approx \kappa \exp(w) \quad (\text{S38})$$

and

$$H_{\text{min}}^{\text{eff}} = \frac{H_{\text{min}}^{\text{micro}} + wH}{1 + w} = H_{\text{min}}^{\text{micro}} + \frac{w}{1 + w}(H - H_{\text{min}}^{\text{micro}}). \quad (\text{S39})$$

By defining

$$\omega := \frac{w}{1 + w} \quad (\text{S40})$$

we see that the effective curvature is a weighted average of the original preferred curvature and the current curvature,

$$H_{\text{min}}^{\text{eff}} = (1 - \omega)H_{\text{min}}^{\text{micro}} + \omega H, \quad (\text{S41})$$

with the weight ω increasing with the combined factor $A\phi$. The effective curvature shifts from $H_{\text{min}}^{\text{micro}}$ to H as the coat grows and closes, and the stiffening grows exponentially with this same combined factor. Both effects are caused by the same underlying geometric constraint, which is captured by the single variable w . For the effective energy minimizing curvature, plotting $(H_{\text{min}}^{\text{eff}} - H_{\text{min}}^{\text{micro}})/(H - H_{\text{min}}^{\text{micro}})$ against $w/(1 + w)$ should result in a straight line from the origin with slope one. Looking at the factor w , we see that the stiffness does not scale with closure alone, but with the combined factor $A\phi$. The stiffening and the shift in preferred curvature are caused by both the growth of the coat and the increase of closure. A coat of any size that remains flat ($\phi = 0$) does not show geometric stiffening, and a highly closed coat with very small area stiffens only weakly.

1.3 Phenomenological extension to variable curvature during growth.

We now extend the fixed-growth-curvature result to the case where the membrane curvature changes while new lattice material is incorporated. We do not attempt to derive the full history-dependent elastic problem here. Instead, we use the fixed-curvature result as a local building block and postulate that the connected coat can be decomposed into material increments, or “rings”, that each contribute a quadratic dilation penalty, which also gives a compact notation for cutting experiments.

Let ring i denote a small material increment of area ΔA_i . Let A be the final coat area at which the effective stiffness is measured. The ring is assumed to have been incorporated, or mechanically locked, when the coat had curvature H_i . If the coat is later evaluated at curvature H' , the relative curvature strain associated with this ring is $e_i(H') = -(H' - H_i)/H_i$, in the same small-strain sense used above. We then postulate the ring contribution

$$\frac{\mathcal{U}_{\text{dil},i}}{L_0^2} = \frac{\Delta A_i}{A} \frac{8\mu^2}{KL_0^2} \phi^2 \frac{(H' - H_i)^2}{H_i^2} = \mu w_i (H' - H_i)^2, \quad (\text{S42})$$

with the ring weight

$$w_i := \frac{\Delta A_i}{A} \frac{8\mu}{KL_0^2} \frac{\phi^2}{H_i^2}. \quad (\text{S43})$$

Here H_i is the curvature at which the material increment was incorporated, whereas ϕ is the closure of the coat at the state where the effective response is evaluated. Thus the curvature memory of each ring is set by its birth curvature H_i , but the geometric stiffening amplitude is controlled by the current compactness of the whole coat. This convention recovers the fixed-growth-curvature result when all material increments are incorporated and evaluated at the same curvature.

The full coat energy is

$$\frac{\mathcal{U}_{\text{coat}}(H')}{L_0^2} = \mu(H' - H_{\min}^{\text{micro}})^2 + \mu \sum_i w_i (H' - H_i)^2. \quad (\text{S44})$$

This expression is a sum of quadratic terms in the evaluation curvature H' and can therefore be completed exactly. We define the total stiffening weight and the normalized curvature memory as

$$\mathcal{W} := \sum_i w_i, \quad \mathcal{H} := \frac{\sum_i w_i H_i}{\sum_i w_i}. \quad (\text{S45})$$

Substituting these definitions into Eq. (S44) gives

$$\begin{aligned} \frac{\mathcal{U}_{\text{coat}}(H')}{L_0^2} &= \mu \left[(1 + \mathcal{W})(H')^2 - 2H'(H_{\min}^{\text{micro}} + \mathcal{W}\mathcal{H}) + H_{\min}^{\text{micro}^2} + \sum_i w_i H_i^2 \right] \\ &= \mu(1 + \mathcal{W}) \left[H' - \frac{H_{\min}^{\text{micro}} + \mathcal{W}\mathcal{H}}{1 + \mathcal{W}} \right]^2 + \text{const.} \end{aligned} \quad (\text{S46})$$

The variable-curvature extension therefore predicts

$$\kappa_{\text{cl}}^{\text{eff}} = \kappa_{\text{cl}}(1 + \mathcal{W}) \approx \kappa_{\text{cl}} \exp(\mathcal{W}) \quad (\text{S47})$$

and

$$H_{\min}^{\text{eff}} = \frac{H_{\min}^{\text{micro}} + \mathcal{W}\mathcal{H}}{1 + \mathcal{W}}. \quad (\text{S48})$$

Eq. (S48) can be rewritten as

$$H_{\min}^{\text{eff}} = H_{\min}^{\text{micro}} + \frac{\mathcal{W}}{1 + \mathcal{W}} (\mathcal{H} - H_{\min}^{\text{micro}}). \quad (\text{S49})$$

With

$$\omega := \frac{\mathcal{W}}{1 + \mathcal{W}}, \quad (\text{S50})$$

this becomes

$$H_{\min}^{\text{eff}} = (1 - \omega)H_{\min}^{\text{micro}} + \omega\mathcal{H}. \quad (\text{S51})$$

Thus the effective preferred curvature is a weighted average between the microscopic preferred curvature and the growth curvatures memorised by the material increments. The weights are not

simple area weights: through Eq. (S43) they contain the current closure ϕ , the fractional area contribution $\Delta A_i/A$, and the curvature scale at incorporation.

The fixed-growth-curvature result is recovered as a consistency check. If all material increments are incorporated at the same curvature, $H_i = H_{\text{growth}}$, and the response is evaluated at that same curvature, then

$$\mathcal{W} = \sum_i \frac{\Delta A_i}{A} \frac{8\mu}{KL_0^2} \frac{\phi^2}{H_{\text{growth}}^2} = \frac{8\mu}{KL_0^2} \frac{\phi^2}{H_{\text{growth}}^2} = w. \quad (\text{S52})$$

In the same limit, $\mathcal{H} = H_{\text{growth}}$ and Eq. (S51) reduces to the fixed-curvature expression in Eq. (S39).

For comparison with simulation data, Eq. (S49) suggests the transformation

$$\frac{H_{\text{min}}^{\text{eff}} - H_{\text{min}}^{\text{micro}}}{\mathcal{H} - H_{\text{min}}^{\text{micro}}} = \omega = \frac{\mathcal{W}}{1 + \mathcal{W}}. \quad (\text{S53})$$

The exact ring-weighted growth curvature \mathcal{H} is a history-dependent quantity. When only the final growth curvature is used as a proxy, the collapse should therefore be interpreted as a phenomenological test of the predicted trend rather than as a direct parameter-free measurement of Eq. (S53).

1.4 In the context of non-Euclidean plates

While our case is very specific, the general framework we are dealing with can be understood in the context of a series of papers by Efrati, Sharon and Kupferman on non-euclidean plates [1, 7], which were preceded by the work of Klein et al. on swelling gels [4]. We will now partially summarize and explain their results in the context of our work.

When talking about deformations of shapes, one usually assumes that the shape has a rest configuration described by its positions $\mathbf{x} \in \Omega$. After deformation, the positions are mapped to the deformed state $\mathbf{r}(\mathbf{x})$. The difference between these two states can be quantified using the metric tensors describing each shape. For two points, \mathbf{x} and $\mathbf{x} + d\mathbf{x}$, their distance initially is given by

$$ds_{\text{init}}^2 = \bar{g}_{ij} dx^i dx^j \quad (\text{S54})$$

where \bar{g} is called the rest-metric. After deformation, the point \mathbf{x} is mapped to $\mathbf{r}(\mathbf{x})$, while $\mathbf{x} + d\mathbf{x}$ is mapped to $\mathbf{r}(\mathbf{x} + d\mathbf{x}) \approx \mathbf{r}(\mathbf{x}) + \partial_i \mathbf{r} dx^i$. The distance between these two points in the deformed state is

$$ds_{\text{def}}^2 = |d\mathbf{r}|^2 = dx^i dx^j \partial_i \mathbf{r} \cdot \partial_j \mathbf{r} \equiv dx^i dx^j g_{ij} \quad (\text{S55})$$

which defined the deformed metric g . All deformation information, except for global translations and rotations, is captured in the difference of the metrics, and one defines the strain tensor as

$$\epsilon_{ij} = \frac{1}{2}(g_{ij} - \bar{g}_{ij}). \quad (\text{S56})$$

Often, one sees the following simplification. If we look at a 3d shape, it is always possible to define $\bar{g}_{ij} = \delta_{ij}$, so that the rest-metric is the euclidian metric. For this, the rest-coordinates are simply chosen to be the euclidian coordinates of the 3d embedding space. Then, we reduce to

$$\epsilon_{ij} = \frac{1}{2}(g_{ij} - \delta_{ij}). \quad (\text{S57})$$

Crucially, this simplification works only for a *flat* rest geometry (e.g. a 3d body, a codimension-zero chunk of Euclidean space). For a curved 2d surface like our coat it is impossible: a sphere has no global Euclidean 2d coordinates (theorema egregium), and this very obstruction is the origin of the residual strain.

Under the assumption that the energy is only a function of strain, its lowest order expansion needs to be of the form

$$\mathcal{U} = \frac{1}{2} A^{ijkl} \epsilon_{ij} \epsilon_{kl} \quad (\text{S58})$$

where A^{ijkl} is the elastic tensor. With regard to symmetries and isotropy, it is possible to find the generic form of the elastic tensor, which is where the bulk and shear moduli enter. The important note however is that the energy is a function of the strain.

Usually, the rest-metric \bar{g} is computed from a rest-state. Efrati, Sharon and Kupferman now proposed that one can relax this constraint, and simply *assume* a rest metric \bar{g} . Importantly, while every shape defines a metric, not every metric defines a shape! Such metrics that define "impossible" shapes are called non-immersible. Their example is a flat disc out of a gel that expands upon heating. If one now only heats the center of the disc, this part wants to expand, while the outer part does not. Every tiny patch of disk *has* a rest configuration. However the collection of patches cannot assume a shape that satisfies all rest configurations at the same time. In this case, there exists a rest-metric \bar{g} , that however does not match any shape.

They mention that two very common routes where such a situation can occur are swelling, like in the example above, or assembly at different geometries, like in our clathrin case. [7] Patches of clathrin assemble at a geometry, which defines their patch-rest-metric. However, as curvature changes, newer patches are included at a different rest-metric. This history-dependent reference geometry is precisely the elastic "memory" of non-Euclidean sheets, and is what we report as the coat's *curvature memory*. [7] This can be seen quite well in our case. The only parameter that differentiates geometries is the curvature H , which is related to the Gaussian curvature $K = H^2$. The famous theorema egregium states that this curvature is an intrinsic property of the geometry. A coat assembled at H and forced to H' cannot do this without stretching. Said differently, there is no shape of the spherical cap that can match $g = \bar{g}$, and residual strain will always be present, leading to the source term $2e/\lambda^2$ in our Helmholtz equation.

Two further remarks place our model precisely within this framework. First, because our coat is constrained to a spherical-cap geometry, it cannot relieve the curvature mismatch by buckling out of that family: the out-of-plane (buckling) branch of non-Euclidean plate theory is excluded by construction, and only the in-plane stretching response – our dilation field – remains. Second, the Helfrich-type bending term κH^2 used in our energy landscape is itself the non-Euclidean-plate bending content: for an isometric (stretch-free) configuration it equals the Willmore functional, which for a spherical cap reduces to $\int H^2 dA = H^2 A$. [1]

In a newer work, Meiri and Efrati show that shapes with incompatible metrics will show a super-extensive energy scaling with system size. [6]. Many systems exhibit an energy scaling $E \propto M$ that is linear in the system size, which is called "extensive". Usually, a system consists of small units, and every unit adds some constant energy. Super-extensive scaling means that $E \propto M^\lambda$ with $\lambda > 1$. This means that every unit also increases its own energy with system size, and is to be expected if frustration accumulates in systems with metric-incompatibility.

Assume that the strain $\epsilon = \frac{1}{2}(g - \bar{g})$ is minimized, but not zero everywhere. Then we can expand

ϵ in powers of the system size:

$$\epsilon = \epsilon_{00} + \epsilon_{01}x + \epsilon_{10}y + \epsilon_{11}xy + \dots \quad (\text{S59})$$

Let ϵ_{ij} be the first non-zero term in this expansion, and call $\eta := i + j$. Then the energy will scale like

$$E \sim \int d^d r \epsilon^2 \sim r^d r^{2\eta} \sim M^{1+\frac{2\eta}{d}} \quad (\text{S60})$$

with $M \sim r^d$ being the system size. In our case, we are dealing with a 2d coat, so $d = 2$ and the system size $M = A$ is the area. To find η , remember that by definition

$$g = \bar{g} + 2\epsilon \quad (\text{S61})$$

The constant and linear coefficients $\epsilon_{00}, \epsilon_{01}, \epsilon_{10}$ are compatible (they derive from a displacement) and are set to zero by energy minimization. The first coefficient that cannot be removed is fixed by the metric incompatibility, i.e. the Gaussian-curvature mismatch; and since K is computed from the *second* derivative of the metric (theorema egregium), this obstruction enters at second order. Therefore $\eta = 2$ and we find

$$E \sim A^3. \quad (\text{S62})$$

If we compare to our result that the dilation scales as $\Xi \sim A$ (at fixed H , since $\Xi \propto \phi$ and $\phi \propto A$), and that the total energy is the energy density $\propto \Xi^2$ times the area, $E \sim A \Xi^2$, we find $E \sim A^3$ – in agreement with the super-extensive scaling.

1.5 Geometry and invagination energy landscape

Geometry calculations

A spherical cap is parameterized by its mean curvature $H = 1/R$ and its closing angle $\vartheta \in [0, \pi]$. The surface area of the cap is

$$A(H, \vartheta) = \frac{2\pi}{H^2}(1 - \cos \vartheta). \quad (\text{S63})$$

The *closure* ϕ measures the fraction of a full sphere covered by the cap,

$$\phi = \frac{AH^2}{4\pi} = \frac{1 - \cos \vartheta}{2} \in [0, 1]. \quad (\text{S64})$$

For the surface-tension contribution to the invagination energy (Sec. 1.5), we need the excess area relative to the flat disc of the same projected radius,

$$\Delta A = A - \pi R^2 \sin^2 \vartheta = A \frac{1 - \cos \vartheta}{2} = \frac{A^2 H^2}{4\pi}. \quad (\text{S65})$$

Invagination energy landscape

In the main text we use a reduced two-variable description of the invagination process. The state of the pit is described by the membrane area A covered by the coat and by the mean curvature H of the corresponding spherical cap. This landscape is not meant to be the microscopic simulation Hamiltonian. Instead, it is an effective coarse-grained energy landscape in which microscopic lattice degrees of freedom, membrane shape modes beyond the spherical-cap approximation, and local relaxation processes have been absorbed into a small number of effective parameters. Within this reduced description, the invagination is described by the systems state $s = (H, A)$ which changes according to the underlying energy landscape. The ground for that is an a-priori *static* energy landscape $E(H, A, s)$, which depends on the curvature of the system, its area and changeable system parameters, like the clathrin bending rigidity or the preferred curvature.

In the spherical cap model, the accessible domain is the region in the (H, A) plane with closure $\phi \leq 1$, which corresponds to the geometric constraint that a spherical cap of curvature H cannot have an area larger than $A_{\max}(H) = 4\pi/H^2$.

$$0 \leq \phi = \frac{AH^2}{4\pi} \leq 1, \quad A \leq A_{\max}(H) = \frac{4\pi}{H^2}. \quad (\text{S66})$$

The $\phi = 1$ boundary will be essential for the understanding of the state trajectories in the energy landscape. We will show that the energy minimum in this landscape, the *attractor*, moves during maturation of the coat, which is what determines the shape of the state-trajectory through the (H, A) plane. The state is "chasing" its attractor. If the attractor is "caught" inside the accessible state space, the pit becomes aborted. If the attractor moves outside the accessible region before being caught, the pit closes.

The landscape contains four contributions: membrane bending, membrane surface tension, clathrin polymerization, and clathrin bending. These terms should be read as an instantaneous effective description of a coat at a given stage of assembly. In particular, the clathrin parameters introduced below are the effective parameters generated by the lattice state discussed in the previous sections. A well established result in the literature is that a spherical closed membrane has bending energy $4\pi\kappa_M$, irrespective of its size (depending on convention, a factor of 2 might be different). We will use this energy scale to normalize all energy contributions to work in dimensionless units. We write

$$\mathcal{E}(H, A) := \frac{E(H, A)}{4\pi\kappa_M}. \quad (\text{S67})$$

Here κ_M is the membrane bending rigidity. With the curvature convention used throughout this supplement, the membrane bending term is

$$E_{\text{bend}} = \kappa_M H^2 A, \quad \mathcal{E}_{\text{bend}} = \frac{AH^2}{4\pi} = \phi. \quad (\text{S68})$$

Thus membrane bending penalizes curvature and contributes exactly the closure coordinate in the normalized landscape.

The membrane tension term is the work required to create excess membrane area relative to the flat projected disc. Using Eq. (S65),

$$E_{\text{tens}} = \sigma \Delta A = \sigma \frac{A^2 H^2}{4\pi}, \quad \mathcal{E}_{\text{tens}} = \frac{\sigma}{\kappa_M} \frac{A^2 H^2}{(4\pi)^2}. \quad (\text{S69})$$

Both membrane bending and membrane tension are minimized at the origin of the (H, A) plane and therefore oppose invagination.

The clathrin polymerization term accounts for the free-energy gain of adding triskelia to the coat. If $\Delta E_{\text{pol}} > 0$ denotes the average free-energy gain per incorporated triskelion and A_{cl} is the average area per triskelion in the assembled lattice, then

$$E_{\text{pol}} = -\Delta E_{\text{pol}} \frac{A}{A_{\text{cl}}}, \quad \mathcal{E}_{\text{pol}} = -\frac{\Delta E_{\text{pol}}}{4\pi\kappa_{\text{M}}} \frac{A}{A_{\text{cl}}}. \quad (\text{S70})$$

This term favors increasing coat area, driving the system away from the origin. In contrast to the stiffness calculation above, the factor A_{cl} is used here only to convert coat area into an approximate number of incorporated triskelia.

The final term is the clathrin bending energy. Here we explicitly use the effective bending rigidity and effective preferred curvature of the clathrin coat. To keep this distinction visible in the equations, we denote them by $\kappa_{\text{cl}}^{\text{eff}}$ and $H_{\text{min}}^{\text{eff}}$,

$$E_{\text{cl}} = \kappa_{\text{cl}}^{\text{eff}} (H - H_{\text{min}}^{\text{eff}})^2 A, \quad \mathcal{E}_{\text{cl}} = \frac{\kappa_{\text{cl}}^{\text{eff}}}{4\pi\kappa_{\text{M}}} (H - H_{\text{min}}^{\text{eff}})^2 A. \quad (\text{S71})$$

This term favors curvatures close to $H_{\text{min}}^{\text{eff}}$ and becomes more important as the coat grows. The quantities $\kappa_{\text{cl}}^{\text{eff}}$ and $H_{\text{min}}^{\text{eff}}$ are coarse-grained, state-dependent quantities. They correspond to the effective coat rigidity and effective energy minimizing curvature derived above, evaluated for the current lattice state and growth history. In the main text, varying $\kappa_{\text{cl}}^{\text{eff}}$ is a compact way to show how the stiffening mechanism shifts the energy basin. For analytic clarity we treat $\kappa_{\text{cl}}^{\text{eff}}$ and $H_{\text{min}}^{\text{eff}}$ as fixed parameters when minimizing a single instantaneous landscape.

Combining the four terms gives

$$\mathcal{E}(H, A) = \frac{AH^2}{4\pi} + \frac{\sigma}{\kappa_{\text{M}}} \frac{A^2 H^2}{(4\pi)^2} + \frac{\kappa_{\text{cl}}^{\text{eff}}}{4\pi\kappa_{\text{M}}} (H - H_{\text{min}}^{\text{eff}})^2 A - \frac{\Delta E_{\text{pol}}}{4\pi\kappa_{\text{M}}} \frac{A}{A_{\text{cl}}}. \quad (\text{S72})$$

This is the energy landscape shown in Fig. 5 of the main text. When the coat stiffens during assembly, Eq. (S72) should be interpreted quasi-statically: at each stage the current lattice connectivity and growth history determine the effective values of $\kappa_{\text{cl}}^{\text{eff}}$ and $H_{\text{min}}^{\text{eff}}$, and the landscape describes the direction in which the coarse variables H and A are biased at that stage.

For a fixed coat area A and fixed instantaneous values of $\kappa_{\text{cl}}^{\text{eff}}$ and $H_{\text{min}}^{\text{eff}}$, the curvature of the local energy minimum is obtained from $\partial_H \mathcal{E} = 0$. Differentiating Eq. (S72) gives

$$\partial_H \mathcal{E} = \frac{AH}{2\pi} + \frac{\sigma}{\kappa_{\text{M}}} \frac{A^2 H}{8\pi^2} + \frac{\kappa_{\text{cl}}^{\text{eff}}}{2\pi\kappa_{\text{M}}} A (H - H_{\text{min}}^{\text{eff}}). \quad (\text{S73})$$

Solving for H gives the preferred landscape curvature H^* :

$$H^*(A) = \frac{4\pi\kappa_{\text{cl}}^{\text{eff}} H_{\text{min}}^{\text{eff}}}{A\sigma + 4\pi(\kappa_{\text{cl}}^{\text{eff}} + \kappa_{\text{M}})}. \quad (\text{S74})$$

Increasing membrane tension shifts this trajectory to lower curvature, while increasing effective clathrin stiffness shifts it toward $H_{0,\text{cl}}^{\text{eff}}$.

Growth however is mainly controlled through the coat area A . Growth is only limited if an energy minimum exists at a finite area. By plugging in the energy minimising curvature H^* into the combined energy, we reach an effective one-dimensional energy

$$\mathcal{E}^*(A) := \mathcal{E}(H^*(A), A) \quad (\text{S75})$$

and can check if it has a stationary point at positive area. The resulting critical area (discarding the negative area solution) is

$$A_{\text{crit}} = \frac{4\pi\kappa_M}{\sigma} \left[\frac{H_{\text{min}}^{\text{eff}} (\kappa_{\text{cl}}^{\text{eff}}/\kappa_M) \sqrt{A_{\text{cl}}} \sqrt{\kappa_M + \kappa_{\text{cl}}^{\text{eff}}}}{\sqrt{A_{\text{cl}} (H_{\text{min}}^{\text{eff}})^2 \kappa_{\text{cl}}^{\text{eff}} - \Delta E_{\text{pol}}}} - \left(1 + \frac{\kappa_{\text{cl}}^{\text{eff}}}{\kappa_M} \right) \right]. \quad (\text{S76})$$

The corresponding curvature at that critical area is

$$H_{\text{crit}} = \frac{\sqrt{A_{\text{cl}} (H_{\text{min}}^{\text{eff}})^2 \kappa_{\text{cl}}^{\text{eff}} - \Delta E_{\text{pol}}}}{\sqrt{A_{\text{cl}}} \sqrt{\kappa_M + \kappa_{\text{cl}}^{\text{eff}}}}. \quad (\text{S77})$$

Equivalently, with the membrane tension length $\ell_\sigma^2 := \kappa_M/\sigma$, Eq. (S76) can be written as

$$A_{\text{crit}} = 4\pi\ell_\sigma^2 \left[\frac{\kappa_{\text{cl}}^{\text{eff}}}{\kappa_M} \left(\frac{H_{\text{min}}^{\text{eff}}}{H_{\text{crit}}} - 1 \right) - 1 \right]. \quad (\text{S78})$$

Equations (S76) and (S77) give a criterion for when the landscape contains an energy basin. Such a basin exists only if H_{crit} exists, is real, and A_{crit} is positive.

The critical curvature is real only if

$$\Delta E_{\text{pol}} < \Delta E_{\text{max}} := A_{\text{cl}} (H_{\text{min}}^{\text{eff}})^2 \kappa_{\text{cl}}^{\text{eff}}. \quad (\text{S79})$$

The critical area is positive only if the polymerization gain is large enough,

$$\Delta E_{\text{pol}} > \Delta E_{\text{min}} := \frac{A_{\text{cl}} (H_{\text{min}}^{\text{eff}})^2 \kappa_{\text{cl}}^{\text{eff}}}{1 + \kappa_{\text{cl}}^{\text{eff}}/\kappa_M}. \quad (\text{S80})$$

Thus a finite basin in the accessible instantaneous landscape requires

$$\Delta E_{\text{min}} < \Delta E_{\text{pol}} < \Delta E_{\text{max}}. \quad (\text{S81})$$

If polymerization is too weak, coat growth is not favorable. If polymerization is too strong relative to clathrin bending stiffness, the energy decreases by adding more clathrin and no finite-area basin arrests growth. Increasing the effective stiffness $\kappa_{\text{cl}}^{\text{eff}}$ raises the upper threshold ΔE_{max} and can therefore create a finite energy basin for a fixed polymerization gain. This is the continuum landscape representation of the stiffening mechanism: as the coat becomes effectively stiffer, and as its effective

preferred curvature changes through H_{\min}^{eff} , the energy minimum moves through the (H, A) plane. If that minimum remains inside the accessible region, the pit can arrest as an aborted pit. If the minimum is displaced beyond the closure boundary $\phi = 1$, the accessible landscape drives the coat toward vesicle closure. These conditions should not be read as sharp microscopic fate boundaries, but as a coarse-grained explanation for how changes in membrane tension, polymerization gain, connectivity, and lattice stiffening reorganize the invagination landscape.

1.6 Coat Cutting

The same notation gives a compact description of in-silico cutting. A cut reduces the mechanical contribution of selected rings or bonds. We represent this by replacing

$$w_i \rightarrow c_i w_i, \quad 0 \leq c_i \leq 1, \quad (\text{S82})$$

where $c_i = 1$ leaves ring i unchanged and $c_i = 0$ removes its contribution to the connected stress-transmitting coat. After cutting,

$$\mathcal{W}_{\text{after}} = \sum_i c_i w_i, \quad \mathcal{H}_{\text{after}} = \frac{\sum_i c_i w_i H_i}{\sum_i c_i w_i}. \quad (\text{S83})$$

The post-cut effective parameters are therefore

$$\kappa_{\text{cl, after}}^{\text{eff}} = \kappa_{\text{cl}}(1 + \mathcal{W}_{\text{after}}) \quad (\text{S84})$$

and

$$H_{\min, \text{after}}^{\text{eff}} = \frac{H_{\min}^{\text{micro}} + \mathcal{W}_{\text{after}} \mathcal{H}_{\text{after}}}{1 + \mathcal{W}_{\text{after}}}. \quad (\text{S85})$$

We define the positive removed weight as

$$\delta \mathcal{W} := \mathcal{W} - \mathcal{W}_{\text{after}} = \sum_i (1 - c_i) w_i > 0. \quad (\text{S86})$$

We will see that the material removed by the cut carries the weighted memorised curvature

$$H_{\text{cut}} := \frac{\sum_i (1 - c_i) w_i H_i}{\sum_i (1 - c_i) w_i} \quad (\text{S87})$$

which we therefore define already here. The post-cut quantities can therefore be written as

$$\mathcal{W}_{\text{after}} = \mathcal{W} - \delta \mathcal{W}, \quad \mathcal{W}_{\text{after}} \mathcal{H}_{\text{after}} = \mathcal{W} \mathcal{H} - \delta \mathcal{W} H_{\text{cut}}. \quad (\text{S88})$$

Within the linearized stiffness expression, cutting lowers the effective bending rigidity by

$$\Delta \kappa_{\text{cl}}^{\text{eff}} = \kappa_{\text{cl, after}}^{\text{eff}} - \kappa_{\text{cl}}^{\text{eff}} = -\kappa_{\text{cl}} \delta \mathcal{W} < 0. \quad (\text{S89})$$

For the preferred curvature, inserting Eq. (S88) into Eq. (S85) gives

$$H_{\min, \text{after}}^{\text{eff}} = \frac{H_{\min}^{\text{micro}} + \mathcal{W} \mathcal{H} - \delta \mathcal{W} H_{\text{cut}}}{1 + \mathcal{W} - \delta \mathcal{W}}. \quad (\text{S90})$$

Subtracting the intact value $H_{\min}^{\text{eff}} = (H_{\min}^{\text{micro}} + \mathcal{W}\mathcal{H})/(1 + \mathcal{W})$ gives the exact finite-cut expression within the same linearized model,

$$\begin{aligned}\Delta H_{\min}^{\text{eff}} &= H_{\min, \text{after}}^{\text{eff}} - H_{\min}^{\text{eff}} \\ &= \frac{\delta\mathcal{W}}{1 + \mathcal{W} - \delta\mathcal{W}} \left(H_{\min}^{\text{eff}} - H_{\text{cut}} \right).\end{aligned}\tag{S91}$$

For a weak cut, $\delta\mathcal{W} \ll 1 + \mathcal{W}$, this reduces to

$$\boxed{\Delta H_{\min}^{\text{eff}} \simeq \frac{\delta\mathcal{W}}{1 + \mathcal{W}} \left(H_{\min}^{\text{eff}} - H_{\text{cut}} \right).}\tag{S92}$$

Cutting increases the effective preferred curvature if the removed material carries a lower memorized curvature than the intact coat, $H_{\text{cut}} < H_{\min}^{\text{eff}}$. This is the typical situation for cuts that remove early material incorporated at low curvature. In that case, the cut both lowers the effective rigidity and erases part of the coat’s low-curvature memory, allowing the relaxed coat to shift toward higher preferred curvature.

2 Simulation code and reproducibility workflow

The numerical model used in this work is implemented as a Python/JAX codebase that accompanies the manuscript. The repository is organised as a script-based research workflow rather than as an installable Python package. Its purpose is to make the simulations, post-processing steps, and figure-generation scripts transparent and reproducible. The public release contains the active simulation and analysis pipeline, a minimal runnable example, and the scripts used to assemble the paper figures. Local development archives, exploratory notebooks, large simulation outputs, and generated figures are intentionally excluded from the tracked release repository.

2.1 Repository organisation

The core simulation code is located in `simulation_code/`. The active entry point for running simulations is `run_simulation_batch.py`, which reads a parameter table and dispatches individual simulations to `simulation_worker.py`. The worker constructs a `Grid` object, runs the kinetic Monte Carlo evolution, and writes the resulting trajectory files. The main model classes and geometry helpers are in `simulation_code/classes/`. The most important files are:

- `classes/grid.py`: the `Grid` class, which owns the full lattice state, membrane geometry, random number generator, kinetic Monte Carlo event logic, energy calculations, local relaxation, and plotting helpers.
- `classes/node.py`: the `Node` class, representing one clathrin triskelion hub with a position, activity state, up to three direct binding partners, and next-nearest-neighborlinks.

- `classes/projection.py` and `classes/helper_methods.py`: geometric and numerical helper routines, including stereographic projection between the sphere and local coordinate charts.
- `classes/face_counting_method.py`: graph-based detection of polygonal motifs such as pentagons, hexagons, and heptagons in the clathrin lattice.
- `calculate_bending_rigidity.py`: post-processing script for extracting an effective coat rigidity and preferred curvature from saved configurations by curvature sweeps and energy fitting.
- `cutting_experiment.py` and `cutting_code_polished.py`: scripts and helper functions for geodesic cutting experiments, topology checks, post-cut relaxation, and before/after rigidity measurements.
- `consolidate_sim_results.py` and `consolidate_cutexp_results.py`: utilities that combine many individual simulation or cutting-experiment folders into compact dictionaries used by the figure-generation scripts.

The repository also contains an `examples/` folder. These examples are not intended to reproduce the full production data set. Instead, they are small end-to-end tests that demonstrate the file layout and show how a new user can run a simulation, read the output, calculate rigidity values, perform a small cutting experiment, consolidate results, and export frames for Blender-based visualization. The paper figure scripts are stored in `figures/`. They operate on consolidated output files generated from the full simulation data sets, which are too large to be stored in the public code repository.

2.2 Representation of the clathrin coat

The coat is represented as a growing graph embedded on a spherical membrane patch. Each active node corresponds to one clathrin hub. Its projected coordinates are stored in a local stereographic chart, while helper functions convert between projected coordinates and three-dimensional points on the sphere whenever geometric distances, tangent vectors, or visualisations are needed. The node state also stores direct nearest-neighborpartners and next-nearest-neighborrelationships. Unoccupied partner slots are represented by sentinel values, so that the node arrays have fixed shapes and can be handled inside JAX-compiled functions.

The `Grid` object stores all global parameters and dynamic state: membrane curvature, preferred curvature, membrane bending rigidity, surface tension, microscopic spring constants, polymerization energies, the random number generator key, the batched node object, and auxiliary matrices such as active-node distance information. Both `Grid` and `Node` are registered as JAX pytrees. Their pytree definitions separate dynamic JAX arrays, which can be traced by JIT-compiled functions, from static Python-side configuration such as node counts, spring constants, and algorithmic settings. This organization is essential for compiling the kinetic Monte Carlo loop while keeping the code close to the physical object model.

2.3 Kinetic Monte Carlo evolution

The central evolution routine is `Grid.evolve_grid_til`. It is implemented with `jax.lax.scan`, so that a complete trajectory of a fixed number of kinetic Monte Carlo steps can be compiled and executed efficiently. At each step, the code constructs the set of currently possible microscopic events, samples one event from the event catalogue, evaluates its energy change, and accepts or rejects the event using a rate- and energy-dependent Metropolis criterion.

The current event catalogue contains five classes of moves: addition of a new node bonded to an available leg of an existing node, formation of a direct nearest-neighborbond, formation of a next-nearest-neighborbond, removal of a direct bond, and removal of a next-nearest-neighborbond. After an accepted or rejected lattice event, the kinetic Monte Carlo time is advanced according to the total event rate. The grid then performs local relaxation moves. In the variable-curvature simulations, the sphere radius can change adiabatically, allowing the membrane patch to invaginate as the lattice grows.

During a batch run, the command-line runner can print controlled progress messages. For example, `--verbose` reports every evolution step in the small example, while `--progress-interval 100` reports only every 100 steps for longer production runs. The first run for a new parameter shape can be slow because JAX compiles the traced computation before executing it.

2.4 Energy terms and recorded observables

The microscopic energy combines membrane and lattice contributions. The membrane part contains a Helfrich bending term and a surface-tension term. The lattice part contains harmonic contributions for bond stretching, in-plane leg angles, out-of-plane leg angles, and next-nearest-neighborgeometry, together with polymerization terms for leg and hub binding. Steric exclusion terms avoid unphysical overlap of nodes. The parameters controlling these contributions are read from a spreadsheet or CSV file by the batch runner.

For each simulation, the code stores a time series of observables in `data_dict.pkl`. The most important entries are the kinetic Monte Carlo time, the sampled process class, the acceptance flag, total energy, active node number, direct and next-nearest-neighborbond numbers, polygon counts, individual energy contributions, acceptance probability, sphere radius, curvature, invagination angle, and membrane area. The final `Grid` object is saved in `grid.pkl`, and the full time-stacked node trajectory is saved in `time_stacked_batched_nodes.pkl`. A human-readable `parameters.txt` file records the parameter row and random seed for each replicate.

The standard output folder for one simulation therefore contains

```
parameters.txt
grid.pkl
data_dict.pkl
time_stacked_batched_nodes.pkl
```

with an additional `calculated_data_dict.pkl` file if post-processing quantities such as bending rigidity have been calculated.

2.5 Bending-rigidity and cutting post-processing

The effective coat rigidity is computed from saved coat configurations. For a chosen timestep, `calculate_bending_rigidity.py` loads the grid and the stored node configuration, imposes a set of nearby curvatures, relaxes internal node coordinates at each curvature, and fits the resulting energy–curvature response. The default output is stored under the key `bending_rigidity` in `calculated_data_dict.pkl`. The same calculation is used inside the cutting workflow to compare the mechanical response before and after a geodesic cut.

The cutting experiment loads a saved simulation folder and defines a geodesic arc on the spherical membrane. Nodes within a specified arc-distance of this geodesic are removed, small disconnected fragments can be discarded, and the remaining coat is relaxed. The workflow records the cut geometry, removed node indices, component sizes, topology-consistency checks, curvature before and after relaxation, and rigidity estimates before and after the cut. This provides the computational basis for perturbing assembled coats and measuring how local connectivity affects the global curvature response.

2.6 Consolidation and figure generation

Large parameter sweeps produce one folder per replicate simulation. To make figure generation independent of the raw folder hierarchy, the helper script `consolidate_sim_results.py` scans a results directory and writes a single `consolidated_sim_results.pkl` file. This file contains three top-level entries: `summary`, a compact list of final observables and parameters for each run; `results`, a dictionary containing the full `data_dict`, optional `calculated_data_dict`, parameters, and source path for each run; and `metadata`, which records the source directory and creation information. The paper figure scripts read these consolidated files rather than scanning raw simulation folders directly.

The public repository includes the figure-generation scripts and small figure-local assets. The full simulation output archive is not tracked because it is large and machine-specific. Consequently, several figure scripts contain local data-path variables that point to the production data archive used for the manuscript. To rerun the figures on another machine, these path variables must be replaced by the corresponding local paths to the consolidated simulation or cutting-experiment results. This separation keeps the code release lightweight while preserving the exact analysis scripts used for the paper figures.

2.7 Reproducibility checks and example workflows

The release repository includes a minimal example that can be run after creating the conda environment specified by `environment.yaml`. The minimal workflow executes a short simulation from a CSV parameter table, writes the standard output files, and plots basic time series from `data_dict.pkl`. Additional examples show how to run a small rigidity calculation, perform a small cutting experiment, consolidate simulation outputs, and export trajectory frames to Blender-friendly `.npz` files. These examples are intentionally small. Their purpose is to verify that the code, file formats, and analysis interfaces work in a fresh checkout; the production simulations used in the paper use larger parameter tables, longer trajectories, and more expensive post-processing settings.

For publication, the repository was tested with a fresh local clone: the conda environment was created from `environment.yaml`, the minimal simulation was run from `examples/01_minimal_simulation/`, the output was analyzed, and the resulting folder was consolidated successfully. Generated output files, JAX compilation caches, local archives, and large data products are ignored by Git. The code is released under the MIT License to permit reuse, modification, and redistribution with attribution.

Caption for Movie S1. Kinetic Monte Carlo simulation of clathrin assembly at fixed membrane curvature of $H = 0.35 L_0^{-1}$. Nodes are colored by their energy from blue (low) to red (high), while bonds are color coded by the number of leg segments coinciding on that bond, from 2 (blue) over 3 (yellow, one next nearest neighbor bond) to 4 (red, two next nearest neighbor bonds).

Caption for Movie S2. Kinetic Monte Carlo simulation of clathrin assembly at fixed membrane curvature of $H = 0.2 L_0^{-1}$. Nodes are colored by their energy from blue (low) to red (high), while bonds are color coded by the number of leg segments coinciding on that bond, from 2 (blue) over 3 (yellow, one next nearest neighbor bond) to 4 (red, two next nearest neighbor bonds).

Caption for Movie S3. Kinetic Monte Carlo simulation of clathrin assembly at variable membrane curvature with surface tension ratio $\sigma/\kappa_M = 0.4$, assembling into a flat plaque. Nodes are colored by their energy from blue (low) to red (high), while bonds are color coded by the number of leg segments coinciding on that bond, from 2 (blue) over 3 (yellow, one next nearest neighbor bond) to 4 (red, two next nearest neighbor bonds).

Caption for Movie S4. Kinetic Monte Carlo simulation of clathrin assembly at variable membrane curvature with surface tension of ratio $\sigma/\kappa_M = 0.2$, assembling into an aborted pit. Nodes are colored by their energy from blue (low) to red (high), while bonds are color coded by the number of leg segments coinciding on that bond, from 2 (blue) over 3 (yellow, one next nearest neighbor bond) to 4 (red, two next nearest neighbor bonds).

Caption for Movie S5. Kinetic Monte Carlo simulation of clathrin assembly at variable membrane curvature with surface tension ratio $\sigma/\kappa_M = 0.025$, assembling into a closed cage. Nodes are colored by their energy from blue (low) to red (high), while bonds are color coded by the number of leg segments coinciding on that bond, from 2 (blue) over 3 (yellow, one next nearest neighbor bond) to 4 (red, two next nearest neighbor bonds).

Caption for Movie S6. Animation of in silico cutting experiment. A previously simulated cage at surface tension ratio $\sigma/\kappa_M = 0.05$, is cut along a geodesic. Afterwards we perform 120,000 Monte Carlo relaxation steps, with the cage increasing its curvature. Bond and node colors encode the local energetic load on a logarithmic scale (blue is low, red is high).

References

- [1] E. Efrati, E. Sharon, and R. Kupferman. Elastic theory of unconstrained non-Euclidean plates. *J. Mech. Phys. Solids*, 57(4):762–775, 2009.
- [2] F. Gittes, B. Mickey, J. Nettleton, and J. Howard. Flexural rigidity of microtubules and actin filaments measured from thermal fluctuations in shape. *J. Cell Biol.*, 120(4):923–934, 1993.
- [3] A. J. Jin and R. Nossal. Rigidity of Triskelion Arms and Clathrin Nets. *Biophys. J.*, 78(3):1183–1194, 2000.

- [4] Y. Klein, E. Efrati, and E. Sharon. Shaping of Elastic Sheets by Prescription of Non-Euclidean Metrics. *Science*, 315(5815):1116–1120, 2007.
- [5] E. M. Lifšic, A. M. Kosevič, L. P. Pitaevskij, E. M. Lifšic, and L. D. Landau. *Theory of Elasticity*. Number 7 in Course of Theoretical Physics / L. D. Landau and E. M. Lifshitz. Pergamon Press, 3., engl. ed., rev. and enl edition, 1986.
- [6] S. Meiri and E. Efrati. Cumulative geometric frustration in physical assemblies. *Phys. Rev. E*, 104(5):054601, 2021.
- [7] E. Sharon and E. Efrati. The mechanics of non-Euclidean plates. *Soft Matter*, 6(22):5693, 2010.